UNIVERSIDADE ESTADUAL DE PONTA GROSSA
SETOR DE CIÊNCIAS EXATAS E NATURAIS
PROGRAMA DE PÓS-GRADUAÇÃO EM CIÊNCIAS

DIOGO LEONAI MARQUES DE SOUZA

SYNCHRONIZATION AND TRAVELING WAVE CLASSIFICATION IN HIPPOCAMPAL NETWORK

SINCRONIZAÇÃO E CLASSIFICAÇÃO DE ONDAS VIAJANTES EM UMA REDE DO HIPOCAMPO

PONTA GROSSA

2024

DIOGO LEONAI MARQUES DE SOUZA

SYNCHRONIZATION AND TRAVELING WAVE CLASSIFICATION IN HIPPOCAMPAL NETWORK

SINCRONIZAÇÃO E CLASSIFICAÇÃO DE ONDAS VIAJANTES EM UMA REDE DO HIPOCAMPO

Dissertation presented to Graduate in Science Program, concentration area Physics, of the Universidade Estadual de Ponta Grossa, as a partial requirement to obtain a Master in Science title.

Advisor: Prof. Dr. Antonio Marcos Batista.

Co-Advisor: Prof. Dr. Kelly Cristiane Iarosz.

PONTA GROSSA

2024

Souza, Diogo Leonai Marques de
S729 Synchronization and traveling wave classification in hippocampal network / Diogo Leonai Marques de Souza. Ponta Grossa, 2024.
65 f.

Dissertação (Mestrado em Ciências - Área de Concentração: Física), Universidade Estadual de Ponta Grossa.

Orientador: Prof. Dr. Antonio Marcos Batista.
Coorientadora: Profa. Dra. Kelly Cristiane Iarosz.

1. Rede neuronal. 2. Sincronização. 3. Ondas viajantes. 4. Hipocampo. 5. Sinapses. I. Batista, Antonio Marcos. II. Iarosz, Kelly Cristiane. III. Universidade Estadual de Ponta Grossa. Física. IV.T.

CDD: 530

Ficha catalográfica elaborada por Maria Luzia Fernandes Bertholino dos Santos- CRB9/986

TERMO DE APROVAÇÃO

DIOGO LEONAI MARQUES DE SOUZA

SYNCHRONIZATION AND TRAVELING WAVE CLASSIFICATION IN HIPPOCAMPAL NETWORK

Dissertação aprovada como requisito parcial para obtenção do grau de Mestre em Ciências, no Programa de Pós-Graduação em Ciências, Área de Concentração em Física Teórica da Universidade Estadual de Ponta Grossa, pela seguinte banca examinadora:

gov.br Documento assinado digitalmente
KELLY CRISTIANE IAROSZ
Data: 01/08/2024 10:37:28-0300
Verifique em https://validar.iti.gov.br

_____

Drª. Kelly Cristiane Iarosz – UNIFATEB/PR – Presidente

gov.br Documento assinado digitalmente
SILVIO LUIZ THOMAZ DE SOUZA
Data: 01/08/2024 10:27:14-0300
Verifique em https://validar.iti.gov.br

_____ _____

Dr. Silvio Luiz Thomaz de Souza – UFSJ/MG– Titular

gov.br Documento assinado digitalmente
MATHEUS ROLIM SALES
Data: 01/08/2024 10:32:38-0300
Verifique em https://validar.iti.gov.br

_____ _____

Dr. Matheus Rolim Sales – UNESP/SP – Titular

Ponta Grossa, 01 de agosto de 2024.

ACKNOWLEDGEMENTS

To the State University of Ponta Grossa, the Graduate Program in Sciences/Physics and the funding agency CAPES.

My deepest gratitude to my advisor, Prof. Dr. Antonio Marcos Batista, for his lessons, assistance and lectures during this period. Your guidance and support have been essential along this journey, and I am grateful for your dedication and belief in my work.

To my co-advisor, Prof. Dr. Kelly Cristiane Iarosz, for her lessons, support, and insights throughout my Master's degree journey. Her dedication and encouragement have inspired me and have helped me grow both personally and professionally.

To Dr. Fernando Borges da Silva, for all his help in the research developed, lessons and many lectures during this Master's degree. His feedback and encouragement have motivated me, helping me through both challenges and successes, to become a better professional.

To the external collaborators Prof. Dr. Iberê Luiz Caldas, Prof. Dr. Ricardo Luiz Viana, Prof. Dr. Dr. H. C. Mult. Jürgen Kurths. Those who contributed to the discussion, development, and improvement of this project.

To the members of my master's defense, Prof. Dr. Silvio Thomaz and Dr. Matheus Rolim Sales and the members of my master's qualification, Prof. Dr. Ervin Kaminski Lenzi and Prof. Dr. Antonio Sérgio Magalhães, for their time dedicated to reading and for their suggestions.

To my parents, Josiene Sueni Berger and Leo Marques de Souza, for always being there for me, in both happy and sad moments, and for their assistance throughout all phases of my life.

To my siblings Karin Adriane de Lima, Robson Gabriel de Lima and Michel Rodrigo de Lima for their support during this period. Special thanks to my sister, Karin Adriane de Lima, for her support, good advice, and constant encouragement throughout my life. Your presence has been invaluable to me

To Adriely Cristina Syperreck Kuff, for being by my side and supporting me throughout my undergraduate and master's degrees.

To the 105 science group laboratory, for all the time spent together, laughs and for giving me a space to develop this work. Prof. Dr. Kelly Cristiane Iarosz, Prof. Dr. Antonio Marcos Batista, Prof. Dr. José Trobia, Prof. Dr. José Danilo Szezech Júnior, Prof. Dr. Ricardo Luiz Viana, Prof. Dr. Vagner dos Santos, Dr. Fernando Borges da Silva, Dr. Paulo Ricardo Protachevicz, MSc. Enrique Chipicoski Gabrick, MSc. Lucas Eduardo Bentivoglio, MSc. Patricio Dias Cardoso dos Reis, Bch. Fátima Elis Cruziniani, Gustavo Alexandre da Silva, and Ana Luiza Bezeluska for all the easy and hard times spent together.

“There are three things all wise men fear: the sea in storm, a night with no moon, and the anger of a gentle man”.
Rothfuss P., The Wise Man’s Fear.

RESUMO

Nesta dissertação, investigamos a influência do raio de conexão e da força de acoplamento na sincronização e no surgimento de ondas viajantes em uma camada excitatória do hipocampo. A atividade elétrica de cada neurônio é determinada pelo modelo integra-e-dispara exponencial com adaptação. Observamos que, para alguns valores do raio de conexão, a força de acoplamento influencia significativamente a dinâmica exibida na rede. Para alguns valores, a sincronização dos potenciais de ação é alcançada, no entanto, ao aumentar a força de acoplamento para valores mais altos a rede começa a exibir atividade de rajada de disparos. Para valores específicos da força de acoplamento, a sincronização de rajada de disparos é observada, estado associado a crises epilépticas. Portanto, o raio de conexão e a força de acoplamento influenciam o padrão de disparo e a sincronização dos potenciais de ação. Um padrão espacial interessante que emerge em nossa rede neuronal são as ondas viajantes. Tais ondas estão presentes em diferentes regiões do cérebro e estão relacionadas a diversas tarefas cognitivas, como informações espaciais e memória. Deste modo, entender os fatores que dão origem a esses fenômenos é crucial para uma melhor compreensão da comunicação cerebral. Observamos que a camada excitatória do hippocampo gera diversos padrões ondas, desde ondas em forma de anel até ondas espirais. O padrão de onda espiral não é totalmente compreendido, no entanto, é teorizado que tal onda modula a ativação e desativação de algumas regiões cerebrais durante tarefas cognitivas específicas. Mostramos que as ondas espirais emergem em nossa rede para uma vasta gama de raio de conexão e força de acoplamento. Motivados pela falta de métodos simples e confiáveis para detectar quantitativamente ondas espirais, desenvolvemos um método novo e confiável baseado em ferramentas de sincronização para medir ondas espirais. Mostramos que os padrões de ondas espirais são fortemente dependentes do raio de conexão e também das condições iniciais consideradas. Mostramos que, para alguns valores de raio de conexão e força de acoplamento, o padrão de onda e os regimes bistáveis síncronos são observáveis.

Palavras-chave: rede neuronal, sincronização, ondas viajantes, hipocampo, sinapses.

ABSTRACT

In this dissertation, we investigate the influence of the radius of connection and the coupling strength on the synchronization and the emergence of traveling waves in a hippocampal layer of excitatory neurons. The electrical activity of each neuron is given by the adaptive exponential integrate-and-fire model. We noticed that for some values of connection radius, the coupling strength greatly influences the dynamics exhibited in the network. For some values spike synchronization is achieved, however, by increasing the coupling strength for higher values the network starts to display bursting activity. For specific values of coupling strength burst synchronization is observed, a state associated with epileptic seizures. Therefore, the radius of connection and coupling strength controls the firing pattern and the synchronization of action potentials. An interesting spatial pattern that emerges in our neuronal network is the traveling waves. Such waves are present in different regions of the brain and are related to diverse cognitive tasks for instance spatial information and memory. Thus, understanding the factors that give rise to such phenomena is crucial for better insight into brain signaling. We observe that the hippocampal excitatory layer generates diverse wave patterns from ring-shaped waves to spiral waves. Spiral wave pattern is not fully understood, however, it is theorized that such wave modulates the activation and deactivation of some brain regions during cognitive tasks. We show that spiral waves emerge in our network for a vast range of connection radius and coupling strength. Motivated by the lack of simple and reliable methods for quantitatively detecting spiral waves we develop a novel and trustworthy method based on synchronization tools for measuring spiral waves. We show that spiral wave patterns are strongly dependent on the radius of connection and also on the initial conditions considered. We show that for some values of radius of connection and coupling strength, wave pattern and synchronous bistable regimes are observable.

Keywords: neuronal network, synchronization, traveling waves, hippocampus, synapses.

ABBREVIATIONS

PDE	partial differential equation
ODE	ordinary differential equation
WWW	World Wide Web
LIF	leaky integrate-and-fire
IF	integrate-and-fire
HH	Hodgkin-Huxley
ISI	interspike-interval
CV	coefficient of variation
A	adaptation index
PS	phase singularity

SYMBOLS LIST

M_{ij}	Elements of the adjacency matrix
$\langle k \rangle$	mean degree
p	probability of connection
$[K]_{\text{in}}$	intracellular concentration
$[K]_{\text{out}}$	extracellular concentration
q	charge
V	electrical potential
T	temperature
k	number of connections
t	time
C	capacitance
I_{ext}	external current
I_C	capacitive current
I_R	resistive current
E_{L}	resting potential
g_{L}	membrane conductance
V_{max}	maximum potential of the membrane
V_{reset}	reset potential
I_{ion}	ionic currents
$\overline{g}_{\text{K}}$	potassium maximum conductance
$\overline{g}_{\text{Na}}$	sodium maximum conductance
n	potassium activation variable
m	sodium activation variable
h	sodium deactivation variable
E_{K}	potassium equilibrium potential
E_{Na}	sodium equilibrium potential
α_n	potassium rate of close to open

β_n	potassium rate of open to close
α_m	sodium rate of open to close
β_m	sodium rate of close to open
α_h	sodium rate of deactivation to activation
β_h	sodium rate of activation to deactivation
Δ_T	slope factor
w	adaptive current
τ_w	time constant of adaptation
a	subthreshold adaptation
ISI	interspike interval
$\overline{\mathrm{ISI}}$	mean interspike interval
F	frequency
σ_ISI	standard deviation of interspike intervals
CV	coefficient of variation
I_i^syn	synaptic current
V_rev^j	reversal potential of neuron j
g_i	synaptic conductance
τ_g	synaptic conductance time constant
g_syn	coupling strength
N	number of elements
R	radius of connection
$\varphi_i(t)$	phase of the neuron i
$\mathrm{Z}(t)$	temporal global Kuramoto order parameter
Z_g	mean global Kuramoto order parameter
$\mathrm{Z}_{i,j}(t)$	temporal local Kuramoto order parameter
$\overline{\mathrm{Z}}_{l,m}$	temporal mean of the local Kuramoto order parameter
Z_L	mean of all Kuramoto order parameter
PS	amount of phase singularities

CONTENTS

1 INTRODUCTION

The nervous system and the brain are subjects that have been extensively studied for many years. The brain is an organ responsible for controlling both conscious and unconscious activities, such as breathing, vision, and thoughts, among many others (1). Firstly, the brain was thought to be a dense mesh of thin filaments (2). After years of study, Santiago Ramón y Cajal proposed that the brain is composed of elementary cells called neurons (2–5). Years later, the excitability of neurons was shown. Nowadays, the concept of neurons composing the brain and controlling the complex and vast activity of animals and humans is well established. Due to the technological advances in different fields, humankind is able to explore and understand different properties of brains and their fundamental unit called neurons (1, 6, 7). The advances in technology have led scientists to understand the physiology and electrophysiology of neurons and also their behavior as a collective system for instance synchronization and waves. These studies have also deepened our understanding of different brain disorders such as epilepsy, Alzheimer and Parkinson's disease. Two hot topics of study in neuroscience are the traveling waves (8–12) and the global synchronization of neurons (13–16). Traveling waves are associated with distinct cognitive tasks such as learning, memory and vision (8). However, excessive synchronization is related to epileptic seizures (14). Therefore, investigating the properties and activities of the brain is essential.

The collective activity of neurons has been a focus of study for a long time in neuroscience due to its relation to healthy and unhealthy brains. In particular, epilepsy is associated with the excessive firing and synchronization of brain regions (7, 13, 14). Such behavior can occur in whole brain regions or smaller areas and the duration of epileptic crises varies from minutes to hours (17–19). Studies have shown that partial epileptic seizures are triggered by the imbalance of excitatory and inhibitory synapses (20). *In vitro* experiments have demonstrated that the suppression of inhibitory and the enhancement in the excitatory synapses cause epileptic crises (21, 22). Another collective activity that has gained attention from scientists is the traveling waves (8–11). They are astounding spatial-temporal patterns that emerge in large brain regions or localized, and their function over the brain functionality is not yet fully understood (8). It was shown that the communication between the neocortex and hippocampus is mediated by traveling waves (9, 11, 23). Especially in the hippocampus, the traveling waves are correlated with the communication of neurons responsible for the encoding of spatial information (10) and also with the long-term memory process (9). Such waves also play a role in modulating the synaptic plasticity (8). Patten T. M. et al. (23) have shown that the properties of traveling waves, such as propagation direction and speed, are correlated with specific cognitive tasks such as reaction speed. In a recent study conducted by Xu, Y. et al(24), the emergence of a traveling wave with the shape of a spiral (spiral wave) has been detected in the brain during resting and cognitive activities. The authors demonstrated that multiple spirals interact regulating the activation and deactivation of functional brain regions. They theorize that these spiral waves

organize complex dynamics in the human brain by modulating healthy and pathological brain activities, and they are intrinsically involved in cognitive processes.

To investigate and deepen our knowledge regarding neuronal activity, different mathematical models were developed to simulate the electrical activity of neurons (25). Among the many models proposed, the most used are the Izhikevich (25, 26), Rulkov map (27), Hodgkin-Huxley (16, 21, 28), Hindmarsh-Rose (29, 30), leaky integrate-and-fire (31, 32) and adaptive exponential integrate-and-fire (AEIF) models (13, 14, 33–35). Some models focus on the detailed description of the diverse mechanisms involved in neuronal activity, for instance, Hodgkin-Huxley model describes the dynamics of the ionic channels present in the neuronal membrane (16, 36). While others emphasize the simple description of the action potentials, for example the integrate-and-fire models and the Rulkov map (37). A model which is simple enough for easy computational application and faithfully describes the mechanisms under the neuronal activity in the adaptive exponential integrate-and-fire (AEIF) model (33, 34, 37). This model is an improvement from the leaky integrate-and-fire model proposed by Lacpique in 1907 (31). Due to the addition of the exponential term and the adaptive current, the AEIF model describes different firing patterns observed in cortical neurons by controlling a few parameters (33). The parameters of the model can be experimentally measured providing more biophysical meaning for the model. As a result of its simplicity and high biological accuracy, we consider the AEIF model for describing the electrical activity of each neuron of our network.

The simulation of brain regions is done by combining complex networks and neuronal models (25), where the nodes of the network are the neurons and the edges connecting the nodes are the synapses (25, 37). Different network topologies have been applied to study the activity of neuronal populations, for instance, random network (13, 14, 16) and biophysical network (38, 39). The interaction between neurons generates a vast set of activities that can be reproduced and investigated by computational modeling (13, 14, 16, 26, 40).

In this work, we consider the biophysical spatial distribution of an excitatory layer in the hippocampus CA1 region (38, 39). The neurons are connected with each neighbor that is within a radius of the connection, where each neuron's electrical activity is given by the AEIF model. We observe the presence of spike and burst[1] firing patterns depending on the coupling strength and the connection radius. A way of evaluating the firing pattern is by considering the distribution of interval between each firing and its coefficient of variation (34). The measurement of global and local synchronization can be done by calculating the Kuramoto order parameter (41). Different works have shown the importance of synchronization and how excessive synchronization is harmful to the brain (1, 7, 16). In the present dissertation, we study the emergence of synchronization and traveling waves by varying the network parameters. We propose a novel method for characterizing a specific type of traveling wave based on the synchronization measurement tools.

This dissertation is organized in the following form: in Chapter 2, we present the funda-

[1] High frequency of firing followed by a silent period in which the neuron does not fire.

mental concepts for neuronal modeling. The first section presents a basic concept regarding dynamical systems. The second section describes basic concepts about complex networks and types of networks. In the third section of Chapter 2, neuron physiology and electrophysiology are presented. In the last section, we present a method for mathematically modeling the electrical activity of neurons, and we also introduce some models. In Chapter 3, we present the methodology applied in developing this work. In the first section, we present the mathematical model considered and describe the network. The second section presents the tools used for the determination of firing patterns and for measuring synchronization. In the last section, the computer setup and the numerical integrator are described. In Chapter 4, we present the results obtained for the neuronal network considered. The first section shows the influence of the network parameters over neuronal synchronization. In the next two sections, we present a novel method for detecting waves and spiral waves in the network and we study the robustness of these waves for different initial conditions. In Chapter 5, we draw our conclusions. In Chapter 6, possible future works to advance this work are discussed.

2 THEORETICAL FUNDAMENTALS

In this chapter, we present basic concepts about dynamical systems, complex networks neuronal physiology, and electrophysiology. Moreover, we derive the mathematical description of the electrical activity of a neuron and describe some famous neuronal models: the Hodgkin-Huxley model and the adaptive exponential integrate-and-fire (AEIF) model.

2.1 DYNAMICAL SYSTEMS

The dynamical system is the subject that studies the time evolution of a given system, where equations are employed to describe the state that the system is and will be, given its initial state (42). The concepts of dynamical systems are employed in diverse scientific fields such as population growth (43), epidemiology (44), cardiac rhythms (45), neuroscience (25, 35) and others (42, 46). Newton employed the motion equations to describe the movement of the Earth around the Sun, given the inverse-square law of gravitational attraction between the bodies. One of the main focuses of dynamical systems was the study of nonlinear oscillators and their applications. Different scientists have ventured into dynamical systems such as Van der Pol, Andronov, Cartwright and others (42). One topic of dynamical systems that has taken the spotlight for a while was chaos, in which the system exhibits aperiodic activity and is sensitive to small changes in the initial conditions (42, 46).

The states of a dynamical system are given by time-dependent and independent variables and they can be described by partial differential equations (PDE), coupled ordinary differential equations (ODE) or maps. The method by which the system is described influences how time and space are perceived in the system, whether they are continuous or discrete. Partial differential equations describe the space, time and the system's state as continuous. Meanwhile, when considering coupled ordinary differential equations the space of the system is discrete and the time and state variables are continuous. Differential equations faithfully describe different phenomena in the world due to their generalization. However, to integrate these equations is necessary to employ numerical methods and the time to solve the equations varies from milliseconds to days. The maps present a discretization of the time and space although the state variables are continuous. The discretization of two variables makes the maps less general than differential equations, however, the computational implementation of maps is faster and easier. Table 2.1 summarizes the differences of the presented models. In this work, we consider a differential equation model that describes the electrical activity of neurons.

2.2 COMPLEX NETWORKS

Networks are groups of elements that are connected to others. The elements that compose a network are denominated vertices or nodes and the line that connects two or more elements

Table 2.1 – Characteristics of each model (42, 46).

Model	Time	Space	State variable	Pros	Cons
PDE	Continuous	Continuous	Continuous	Generalization	Implementation
CODE	Continuous	Discrete	Continuous	Generalization	Time
Maps	Discrete	Discrete	Continuous	Implementation	No generalization

Source: the author.

is known as edges. The nodes and edges have different meanings in each system. For instance, in neuronal networks, the nodes are considered to be neurons while the edges that connect one neuron to another describe the synapses. In epidemiological studies, the nodes can represent different populations and the edges of the way these populations interact (such as roads, streets, and airspace, among others). Figure 1 presents an illustration of a network, where panels (a) and (b) represent undirected and directed edges, respectively. The difference between both edges is the orientation of from and to the information flows.

Figure 1 – Representation of a (a) undirected and (b) directed network. The red circles are the nodes and the blue lines are the edges.

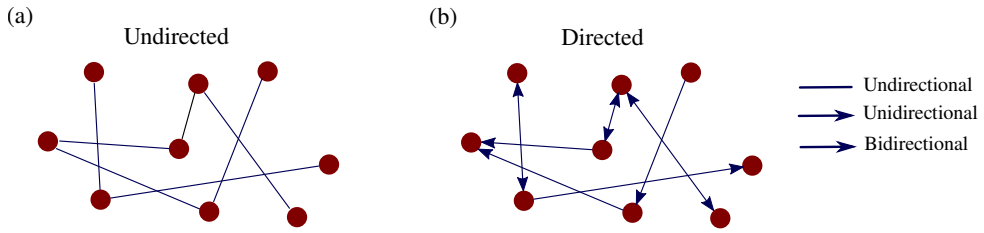

Source: the author.

The study of complex networks started with the graph theory, where both terms network and graph mean the same and they are represented in the same manner with nodes and edges. Paul Erdös and Alfred Rényi (47) proposed a network where the edges were randomly designed using probabilistic tools. After they started describing complex networks as graphs, two different networks were proposed. Duncan Watts and Steven Strogatz (48) developed the "small-world" network and in 1999 and Albert-László Barabási and Réka Albert (49) published their article introducing a "scale-free" network.

In a network, the nodes are usually represented by an index i and the N is the total number of nodes. The structure of the network is represented by the adjacency matrix M and, for a directed network, its elements M_{ij} are given by

$$M_{ij} = \begin{cases} 1, & \text{if element } i \text{ is connected with } j, \\ 0, & \text{if } i \text{ is not connected with } j. \end{cases} \tag{2.1}$$

Here, the network is unweighted meaning that all edges have the same connection weight. One

property of a network is the amount of connection k_i that one element i possess

$$k_i = \sum_{j=1}^{N} M_{ij}, \tag{2.2}$$

with k_i only holding information about a single node of the network. To extend it to the whole network, we calculate the mean number of connections, defined as the mean degree of connection

$$\langle k \rangle = \frac{1}{N} \sum_{i=1}^{N} k_i. \tag{2.3}$$

In the following subsections, we describe in more detail the random, local, small-world and free-scale networks.

2.2.1 Local network

This type of network is part of the regular complex networks due to its symmetric topological organization. In this type of network, the node i only connects to the closest neighbors j. For instance, in a ring-shaped network, the node i connects only with its $i-1$ and $i+1$ nodes. Figure 2 displays a representation of a ring-shaped local network.

Figure 2 – Ring-shaped local network where the first neighbors are coupled.

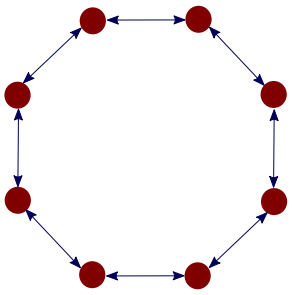

Source: the author.

2.2.2 Random network

The random network proposed by Erdös e Rényi (47), differently from regular networks, does not show a symmetric organization. To construct a random network we first define the number of nodes N, and after that, we connect a node to other elements with a probability p given by

$$p = \frac{k_{\text{Total}}}{N(N-1)}, \tag{2.4}$$

where k_{Total} is the total number of connections in the network and $N(N-1)$ is the maximum number of connections in a network composed of N elements, discarding auto-connections. Figure 3 exhibits a random network for two distinct values of p, where in panel (a) we consider

$p = 0.1$ and in (b) $p = 0.2$. For the cases where $p = 0$ there is no connection in the network while for $p = 1$, the whole network is connected, which is called a global network.

Figure 3 – Representation of a random network for two values of probability of connection, (a) $p = 0.1$ and (b) $p = 0.2$.

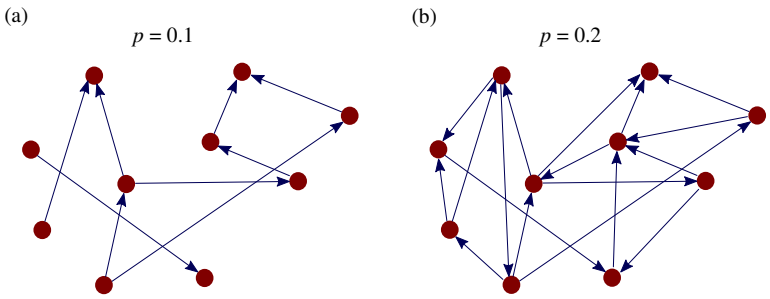

Source: the author.

2.2.3 Small world network

The small world network was inspired by the social studies conducted by Stanley Milgram at Harvard University (50). Milgram's experiment suggests that any two people in the world can be connected by a chain of social connections. He found that the average social chain between two people is around six connections. This social phenomenon was called the "small world". Inspired by Milgram's experiment, two models became famous the Watts-Strogatz (48) and Newman-Watts (51). Both models are depicted in Figure 4. Initially, (a) Watts-Strogatz network is constructed as a regular network of N nodes connected with the closest neighbors. Afterward, each edge is randomly reconnected to a new node with probability p. For $0 < p < 1$, the network exhibits local and non-local coupling. While for $p = 0$, the network is regular and for $p = 1$ we have a random network. (b) The Newman-Watts network does not reconnect the previous nodes from the regular network, they create new connections with other elements with probability p. In this model, for $p = 1$ we obtain a global network.

2.2.4 Scale-free network

The scale-free network was proposed by Barabási and Albert in 1999 (49) while studying the World Wide Web (WWW). The authors showed that a random network is not able to represent the WWW since some nodes of WWW have more edges, Barabási and Albert denominated such nodes as hubs. They also proposed that the number of connections within the network is described by a power law distribution $P(k) = k^{-\gamma}$, where k is the number of connections and γ is the power law coefficient ($2 \leq \gamma \leq 3$). Another important property of scale-free networks is that the network lacks a mean degree of connections due to the great variability of some nodes. Figure 5 displays the topology of such a network.

Figure 4 – Representation of a small-world network proposed by (a) Watts-Strogatz (48) (b) Newman-Watts(51).

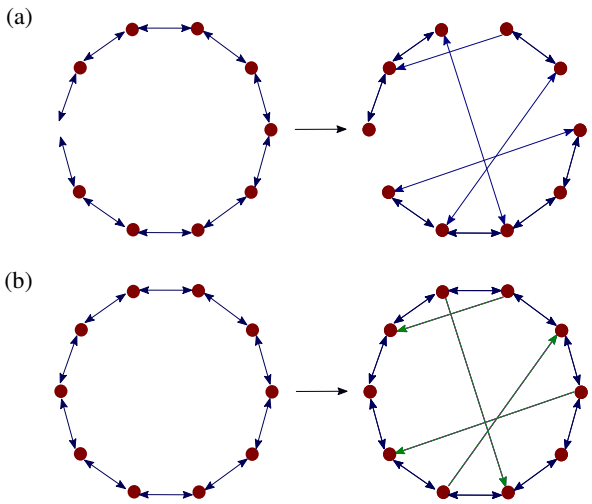

Source: the author.

Figure 5 – Representation of a scale-free network.

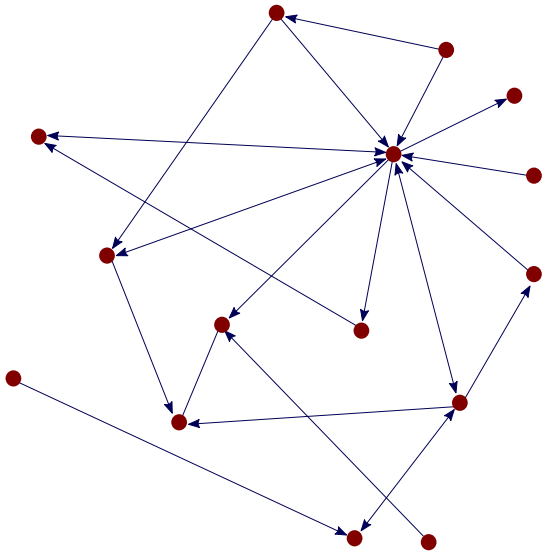

Font: the author.

2.3 NEURONS PHYSIOLOGY AND ELECTROPHYSIOLOGY

In 1871, the researcher German Josef von Gerlach proposed a theory that the brain was composed of a dense mesh of thin filaments that together formed the nerve fibers, this theory was called the “reticular theory” (2). Eleven years later, the “neuron theory” was proposed by Santiago Ramón y Cajal (3–5). He stated that the brain consists of discrete elemental components called neurons (2, 3). Using Golgi stain technique (2, 52) Cajal demonstrates the presence of neurons and their organization in some brain regions (52). The polarization of neurons was also discovered by Cajal and this discovery was entitled “law of dynamic polarization” (3, 5).

Nowadays, it is known that billions of neurons are present in our central nervous system. The total number of neurons is estimated to be 86 billion (6, 53). It is possible to classify neurons based on their morphological structure, such as multipolar, bipolar, pseudo-unipolar, unipolar and others (1, 7, 54). Despite the wide variety of neuron types, it is possible to represent almost all neurons with a simpler model composed of four parts: a receptor, integrator, long-range transmitter and a secretory part. Each component is associated with specific parts of neurons, which is represented in Figure 6. The dendrites (receptor component) are responsible for receiving electrical and chemical impulses from other neurons. The nucleus (secretory component) realizes the protein synthesis of the neuron, whereas the soma (integrator part) processes the signals received by dendrites generating an action potential. The axon (long-range transmitter) transmits the action potential until it arrives at the axon terminals, which connect to other neurons (1, 54, 55). The myelin sheaths wrap the axon to increase the velocity propagation of action potentials through the axon (1, 7).

Figure 6 – Simple representation of a neuron.

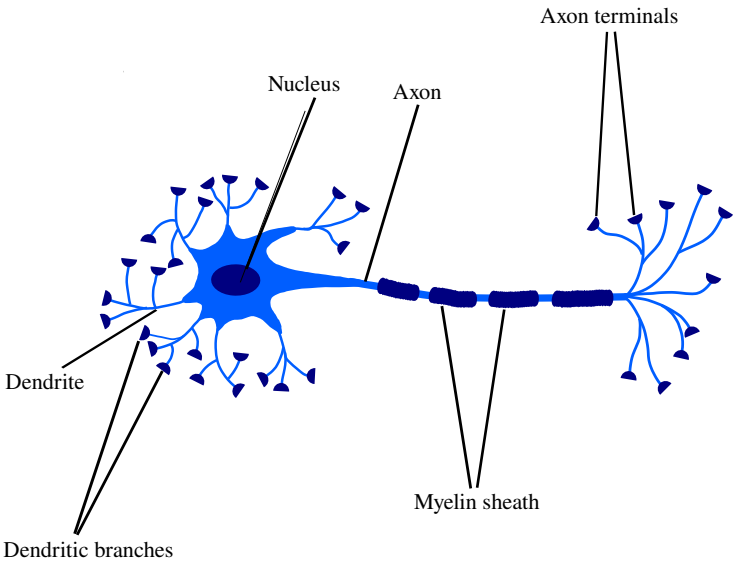

Font: author.

The neuronal membrane consists of a bi-layer of lipids that separates the intracellular (cytoplasm of the cell) from the extracellular fluid (outside medium) (54). Cations and anions are present in the cytoplasm and the extracellular fluid mostly sodium (Na^+), potassium (K^+), calcium (Ca^{2+}) and chloride (Cl^-)(25, 54). These ions are found on either side of the neuronal membrane, however, at different concentrations creating an electrochemical gradient. Na^+, Cl^- and Ca^{2+} are more concentrated in the extracellular medium. The intracellular medium possesses a high concentration of positive ion K^+ and anions usually denoted as A^- (25). The membrane acts as a barrier for the passive diffusion of all ions. However, it is permeable for some ions and the exchange of ions from the extra to intracellular and vice-versa is mediated by ion channels and ion pumps (1). Two types of ion channels are present in neurons: the resting and voltage-gated channels (1, 54), with each type being permeable to different ions. Resting

channels play a role in the passive activity of the membrane, maintaining the neuron in the resting potential for the absence of stimulus (1). Voltage-gated channels are deeply involved in action potential generation. Some channels stay closed while no stimulus arrives at the neuron otherwise, they open allowing the passage of ions through the membrane (1, 6).

At rest, neurons possess a characteristic electric potential value of approximately -75 mV (1). However, a question may arise; how do neurons maintain this electric potential in the absence of stimulus or some kind of battery? To answer this question and others, we first must understand the ionic flux through resting channels. Let us assume an initial state where most K^+ and A^- are in the cytoplasm meanwhile, Na^+ and Cl^- are outside the neuron. The membrane blocks the diffusion of ions, however, there are resting channels that grant passage of a specific type of ion (mostly K^+). Since the resting channels allow diffusion of K^+, there are two possible states for K^+ concentration: inside the neuron ($[K]_{in}$) and outside the neuron ($[K]_{out}$). A well-known equation for physicists can be employed to describe the ratio of outside and inside concentration, the Boltzmann equation (56)

$$\frac{[K]_{out}}{[K]_{in}} = \exp\left(-q\frac{\Delta V}{kT}\right), \tag{2.5}$$

where q is the charge of the ion, ΔV is the difference between inside and outside electrical potential ($V_{in} - V_{out}$), k is the Boltzmann constant and T is the temperature. Applying the natural logarithm to both sides of Equation (2.5), we rewrite it as

$$E_K = -\frac{kT}{q}\ln\left(\frac{[K]_{out}}{[K]_{in}}\right), \tag{2.6}$$

where E_K is the equilibrium potential of K^+. Equation (2.6) is known as Nerst equation (1, 25, 56), and it describes the equilibrium potential where ions stop flowing through resting channels. This equation can also be achieved by using Fick's first law and Ohm's law (25, 57). K^+ diffusion through the resting channels is described by Fick's first law. As more ions flow to the outer region, extracellular K^+ creates an electrical field that blocks the flow of the same ions (25). Table (2.2) shows the concentrations of the most abundant ions inside and outside neurons (1).

Table 2.2 – Concentrations and equilibrium potential of the major type of ions in the Giant Axon of the Squid.

Ion	$[ion]_{inside}$ (mM)	$[ion]_{outside}$ (mM)	Equilibrium potential (mV)
K^+	400	20	-75
Na^+	50	440	+55
Cl^-	52	560	-60
A^-	385	none	none

Font: Adapted from: Kandel, E. R. and Schwartz, J. H. and Jessell, T. M. Principles of Neural Science. Elsevier, 2013, 5th edition.

Voltage-gated channels act differently from resting channels. They open and close depending on the membrane potential of the neuron, where the two abundant voltage-dependent channels are the K^+ and Na^+ (1). These channels are found throughout the entire neuronal membrane and they are the main factor for the generation of action potentials. Figure 7 displays potassium resting channel in yellow, potassium voltage-gated in red and sodium voltage-gated in purple for two situations: the panel (a) shows when the neuron is at rest and the panel (b) when a stimulus is applied to the neuron. In the lack of stimulus (Figure 7 (a)), the voltage-gated channels stay closed and no ion passes through them. Only the resting channel stays open and K^+ ions only pass through this channel to achieve the equilibrium potential. Applying a stimulus to the neuron (Figure 7 (b)) changes the membrane potential and the voltage-dependent channels open for a while. Due to the difference in concentration of some ions, they start to flow to the inside of the neuron. After a while, some channels close and others deactivate, meanwhile the resting channels stay open. The voltage-gated channels play a role in the generation of action potentials in the axon (1, 6).

Figure 7 – Representation of three ionic channels in two different cases. The channels depicted are the resting potassium channel in yellow, the voltage-gated potassium channel in red and the voltage-gated sodium channel in purple. (a) the neuron is at rest and (b) a stimulus is applied to the neuron.

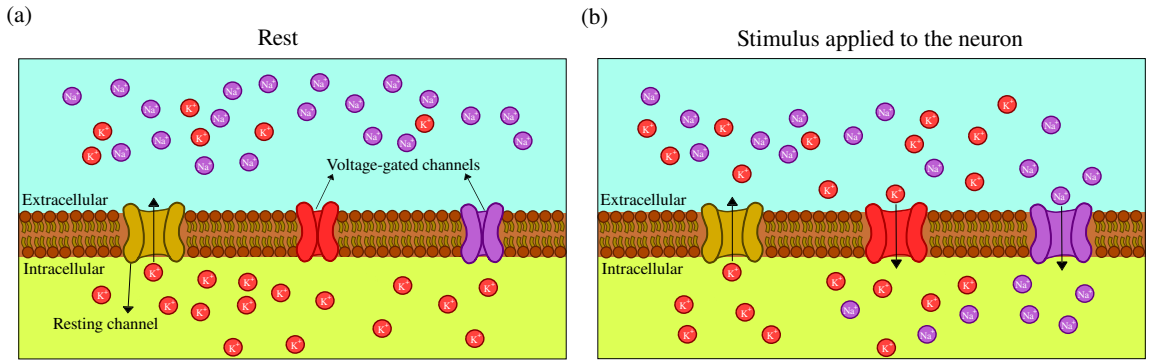

Font: the author.

Action potentials are known as “all-or-none” potentials (25), due to their dependency on the intensity and duration of the stimulus (25, 53). The generation of an action potential is due to the response of K^+ and Na^+ voltage-gated channels to the changes in the intracellular potential. Figure 8 exhibits an action potential of a single neuron. Initially, the neuron is at the resting potential. The application of a current to the neuron increases the membrane potential (V) until it reaches the threshold (25). The threshold potential varies from neuron to neuron however it is usually in the range $[-55, -50]$ mV (58). If the stimulus is not intense or long enough, the membrane potential increases although does not reach the threshold, and therefore, an action potential is not produced. When the threshold is reached, the neuron starts to depolarize. In the depolarization, the Na^+ channels open allowing a fast diffusion of sodium ions to intracellular fluid due to the gradient of concentration, the membrane potential quickly increases and even becomes positive (1, 59). After the peak of the action potential ($V \approx 40$ mV), the sodium

channels are inactivated and the K^+ channels open, initiating the repolarization process. A great amount of potassium ions flow to the inside of the neuron reducing the potential to negative values. Differently from sodium channels, potassium channels do not inactivate and thus, they slowly close which leads to hyperpolarization. In this period, the neuron is less likely to fire a new action potential due to its membrane potential being below the resting potential, and this time interval is denominated as refractory period (53). Other ionic channels play a role in the firing of action potential. For instance, calcium channels (Ca^{+2}) influence the shape of the action potential during the depolarization.

Figure 8 – An action potential of a regular neuron, describing resting (red line), depolarization (blue line), repolarization (magenta line), and hyperpolarization (green line) states. The threshold potential is shown by the black dashed line and the pink vertical dashed lines represent the refractory interval.

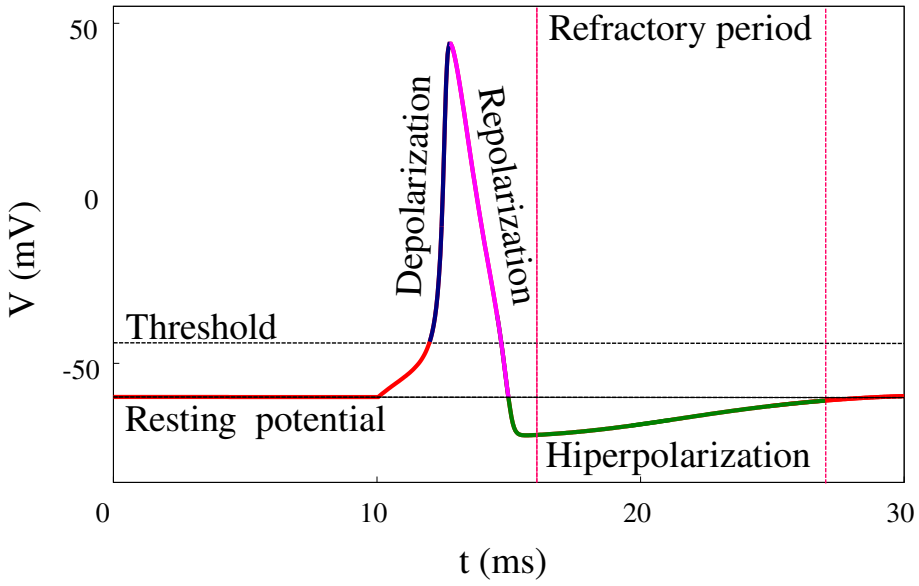

Source: the author.

The action potential propagates through the axon, once it reaches the axonic terminals the neuron communicates with other neurons through synapses (1, 54). The neurons that send and receive the information are denominated as presynaptic and postsynaptic neurons (1, 54, 58), respectively. Two types of synapses can be found in the brain electrical and chemical synapses (54), which are displayed in Figure 9. The electrical synapses (Figure 9 (a)) occur through gap junction channels (54) which are low resistive pathways. This synapse is particularly fast, less than 0.1 ms (54), due to the direct transmission of the information through the gap junction channels. Electrical synapses are bidirectional, where the information can flow from presynaptic to postsynaptic and vice-versa (54). The arrows in the gap junction channels in Figure 9 (a) illustrates this bidirectional property of electrical synapses. In adult mammalian brains, electrical synapses are located in regions where high synchronization is necessary (54).

Chemical synapses (Figure 9 (b)), contrarily from electrical synapses, are located in the whole mammalian brain and are unidirectional (1, 54). This synapse is mediated by neurotransmitters which are stored in synaptic vesicles. The depolarization of the axonic terminals

moves the synaptic vesicles to the neuronal membrane and they fuse after that the fused vesicles abruptly rupture, releasing the neurotransmitters in the synaptic cleft (the gap between pre and postsynaptic neurons) (1). The neurotransmitters cross the synaptic cleft arriving at the postsynaptic receptors, which are responsible for allowing the passage of the neurotransmitters to the cytoplasm of the postsynaptic neuron. The neurotransmitters provoke a change in the membrane potential of the postsynaptic neuron. Depending on the neurotransmitter, the postsynaptic neuron depolarizes or repolarizes. Depolarizing neurotransmitters are classified as excitatory and glutamate is the main excitatory neurotransmitter (1, 54). Meanwhile, repolarizing neurotransmitters are known as inhibitory and γ-aminobutyric (GABA) is the major inhibitory neurotransmitter (54, 59). Neurons are specialized to release only one type of neurotransmitter, either excitatory or inhibitory (1, 60).

Figure 9 – Representation of the (a) electric and (b) chemical synapses. It identifies the main components of each synapse.

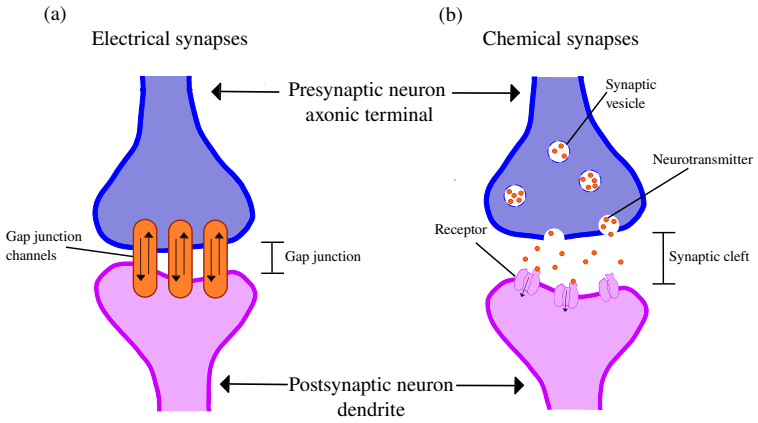

Source: the author.

2.4 MATHEMATICAL NEURON MODELS

Mathematical models are proposed to improve our comprehension of different phenomena and also to predict future states of a system. In the 20th century, the mathematical description of the electrophysiology of neurons has been a hot topic, due to its capability of studying and reproducing an extensive variety of neuronal activity observed *in vivo* (25, 37, 55). For instance, some models that have been widely employed are Hodgkin & Huxley (16, 36), Hindmarsh-Rose (29), Izhikevich (26), Rulkov's map (27), integrate-and-fire (IF) (31) and adaptive exponential integrate-and-fire (AEIF) (14, 33, 35). Despite the uniqueness of each model, it is possible to characterize them into two groups: the ones that seek a simplified description while others describe in detail the mechanisms responsible for an action potential generation (37).

The focus of this section lies in the description and characterization of the adaptive exponential integrate-and-fire (AEIF) model which is used in this dissertation. We also discuss a method for the modeling of the electrical activity of neurons. Moreover, we discuss one of the

most influential neuronal models, the Hodking & Huxley model. Throughout the dissertation, we consider punctual neurons and do not take into account the morphological properties of neurons as well as the propagation of action potentials. We focus on the description of the main electrophysiological characteristics. The models presented in this section are composed of ordinary differential equations (ODE), in which we employ the 4th order Runge-Kutta with constant step $h = 0.05$ ms to integrate them. The simulations in this section were run in the 105 Group Science's lab (table 3.2); unless stated otherwise.

2.4.1 Neuronal modeling

In this subsection, we demonstrate how to mathematically describe the action potential of a single neuron, taking into account the electrophysiology properties of neurons. First, let us consider a single neuron in the brain which is bathed in the extracellular fluid. As discussed in Section 2.2, the intra and extracellular regions possess opposite electrical charges and the neuronal membrane separates both regions (1, 25, 54). This system can be understood as an electrical capacitor of two conductor plates (intracellular and extracellular regions) separated by an insulator (neuronal membrane). The comparison between neurons and capacitors extends to neuron depolarization due to an electrical current, capacitors (similarly neurons) become more positively charged when a current is applied. Hence, it is possible to write the following equation to describe the potential of a neuron when an external current I_{ext} is injected

$$C\frac{dV}{dt} = I_{\text{ext}}, \tag{2.7}$$

where C is the capacitance and V is the potential. This equation is obtained by taking the time derivative of the capacitor equation ($Q = CV$). Equation 2.7 is an oversimplification of the electrical potential of neurons as it does not reproduce the other parts of an action potential or other electrophysiological properties such as the repolarization, resting potential and ion channels. Some of these properties are easily represented as electrical circuit components. The resting potential is equivalent to a battery E_L (with the same potential as the equilibrium potential described by Nerst's equation) and the leaky channels are represented by a resistor R. Figure 10 displays the electrical circuit that represents a neuron. Using the electrical current conservation law we can write

$$I_{\text{ext}} = I_{\text{C}} + I_{\text{R}}, \tag{2.8}$$

where I_{C} is the capacitive current and I_{R} is the current through the resistor. By taking the time derivative of the capacitor equation we have I_{C} given by $I_{\text{C}} = CdV/dt$. Considering that the resistor is ohmic, we can write the current that crosses the resistance as

$$I_{\text{R}} = \frac{(V - E_{\text{L}})}{R}, \tag{2.9}$$

Figure 10 – RC circuit equivalent a neuron electrical activity.

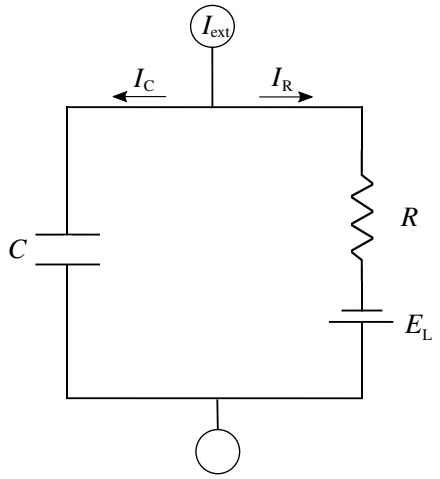

Source: the author.

where E_L is the resting potential and R is the membrane resistance. Replacing I_C and I_R in Equation 2.8, we describe the rate of change of the electrical potential along the time

$$C\frac{dV}{dt} = -g_L(V - E_L) + I_{ext}, \tag{2.10}$$

where g_L is the membrane conductance ($g_L = 1/R$).

In 1907, despite the lack of knowledge about the mechanism behind the firing of action potentials, Louis Lapicque proposed the leaky integrate-and-fire model (LIF) for a single neuron, given by Equation (2.10) (31). He proposed that the neuron can be represented by an RC circuit as discussed in the previous paragraph. However, Equation (2.10) alone cannot fully describe an action potential, leading Lapicque to introduce a reset parameter for V when an action potential is fired (31). When the membrane potential reaches a maximum value ($V \geq V_{max}$), the potential resets to a value $V \rightarrow V_{reset}$, meaning that the capacitor discharges when the potential is equal or greater than a threshold value. The reset parameter can be measured experimentally through voltage traces analysis (61). Figure 11 display the membrane potential as a function of time for Equation (2.10) when no reset condition is applied (panel (a)) and when the reset condition is considered according to Lapicque's model (panel (b)). In panel (a), we observe that the potential increases until it reaches a plateau, and no action potential is produced since the capacitor does not discharge. On the other hand, in panel (b), the consideration of the reset condition generates action potentials. Models that adopt reset mechanisms for the description of repolarization of neurons are known as integrate-and-fire (IF) models (31, 33, 37). Despite the simplification of the repolarization process, these models reproduce several electrical activities observed in both animal and human brains (13, 14, 37, 62).

Including a reset condition to equation 2.10 is one approach to describe the potential of a neuron even though the voltage-gated ionic channels are not considered. Now we take a more

Figure 11 – LIF model when (a) no reset condition is considered and (b) considering the reset condition $V \rightarrow V_{\text{reset}}$ when $V \geq V_{\text{max}}$. We consider the following parameters $C = 280$ pF, $g_{\text{L}} = 12$ nS, $E_{\text{L}} = -70$ mV, $V_{\text{reset}} = E_{\text{L}}$ and $I_{\text{ext}} = 509$ pA (33). Simulation duration = 0.018 s.

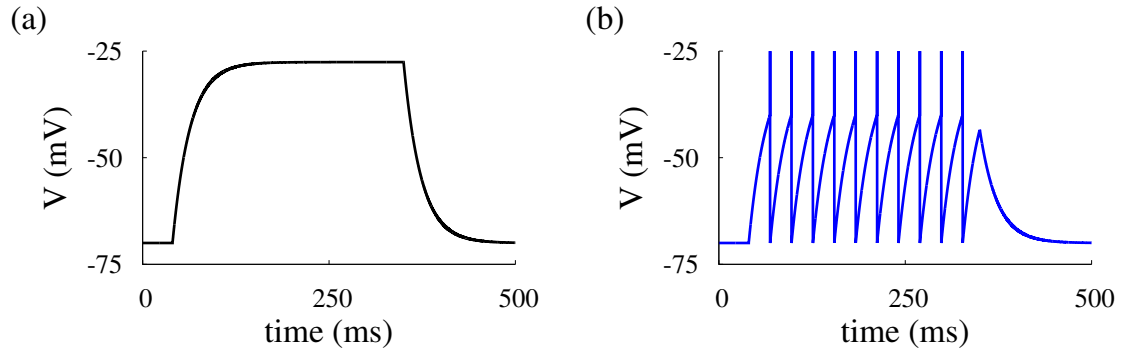

Source: the author.

biophysical approach by starting from Equation (2.10) and adding a current which describes the voltage-gated channels ($I_{\text{ion}}(V)$)

$$C\frac{dV}{dt} = -g_{\text{L}}(V - E_{\text{L}}) + I_{\text{ext}} + I_{\text{ion}}(V). \tag{2.11}$$

Models that describe the dynamics of the voltage-gated channels are known as conductance-base models, and they are mainly influenced by the model proposed by Hodkin and Huxley (36). This approach models not only the membrane potential as well the influence of the channels over the action potential. The biophysical accuracy of such models is superior to IF models, although the computational cost of conductance-based models is higher. In subsection 2.3.2, we describe the Hodgkin-Huxley (HH) model (16, 36).

2.4.2 Hodgkin-Huxley model

Alan Hodgkin and Andrew Huxley were one of the most influential electrophysiologists in the 20th century (1, 25). They started working together in 1935 and published the first measurement of an action potential in history (63). Despite their great success in measuring an action potential, they had to stop their research work due to Hitler's invasion of Poland in World War Two (64). In 1945, Hodgkin and Huxley proposed a method for recording directly the ionic current flow through the membrane of a squid giant axon (axon diameter ≈ 500 µm) (36, 65), a method denominated as patch-clamp (65). Hodgkin and Huxley's research apex was their five publications in 1952 about their mathematical model that mimics the action potentials of a squid giant axon (28, 66–69). They bathed the giant axon in a salt solution and using the patch-clamp technique, they were able to measure the currents through the membrane. During their experiments, they were able to measure the maximum conductance value of the K^+ and Na^+ channels. With this apparatus, they were able to record and mathematically describe the dynamics of potassium and sodium voltage-gated channels in the membrane. Hodgkin-Huxley

(HH) model is a very biophysical accurate model due to the detailed description of the ionic currents present in neurons.

To represent the influence of the voltage-gated channels on the electrical potential of a neuron, Hodgkin and Huxley added two more resistors to represent the potassium current I_K and sodium current I_{Na}. Figure 12 shows the electrical circuit of the HH model. The difference between the LIF and HH circuits is the presence of two resistors. The diagonal arrows across the resistors indicate that the resistance value is not constant. The conductance of the potassium, sodium and leak channels are represented by g_K, g_{Na}, and g_L, respectively. The HH model is

Figure 12 – Hodgkin & Huxley circuit for a squid giant axon.

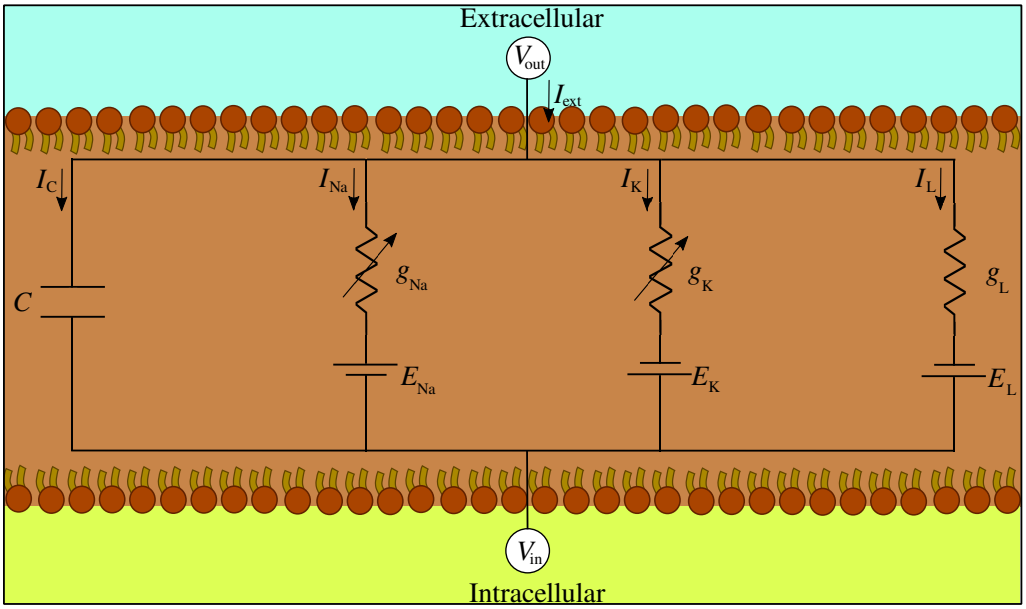

Source: the author

described by four ODEs: one for the membrane potential V, one for the potassium channels activation n, one for the activation of sodium channels m, and the last equation describes the inactivation of sodium channels h. These four ODEs are the following:

$$C\frac{dV}{dt} = -g_L(V-E_L) - \overbrace{\overline{g}_K n^4(V-E_K)}^{I_K} - \underbrace{\overline{g}_{Na} m^3 h(V-E_{Na})}_{I_{Na}} + I_{ext}, \tag{2.12}$$

$$\frac{dn}{dt} = \alpha_n(V)(1-n) - \beta_n(V)n, \tag{2.13}$$

$$\frac{dm}{dt} = \alpha_m(V)(1-m) - \beta_m(V)m, \tag{2.14}$$

$$\frac{dh}{dt} = \alpha_h(V)(1-h) - \beta_h(V)h, \tag{2.15}$$

where C is the capacitance of the membrane, g_L is the leaky conductance, E_L is the rest potential, $\overline{g}_K$ is the potassium maximum conductance, E_K is the equilibrium potential of the potassium ions, $\overline{g}_{Na}$ is the maximum conductance of the sodium ions, E_{Na} is the equilibrium potential of

sodium ions and I_{ext} is the external current applied to the neuron. The variables α and β are the rate at which the channels transition from closed to open and open to closed, respectively. Hodgkin and Huxley described α and β for squid axon as (28)

$$\alpha_n(V) = 0.01\frac{V+10}{\exp(0.1(V+10))-1}, \tag{2.16}$$

$$\beta_n(V) = 0.125\exp\left(-\frac{V}{80}\right), \tag{2.17}$$

$$\alpha_m(V) = 0.1\frac{V+25}{\exp(0.1(V+25))-1}, \tag{2.18}$$

$$\beta_m(V) = 4\exp\left(\frac{V}{18}\right), \tag{2.19}$$

$$\alpha_h(V) = 0.07\exp\left(\frac{V}{20}\right), \tag{2.20}$$

$$\beta_h(V) = \frac{1}{\exp(0.1(V+30))+1}. \tag{2.21}$$

Figure 13 (a) displays the membrane potential V using the HH model and the external current pulse I_{ext} applied to the neuron, where each current pulse has a duration of 2 ms. The panel (b) shows the respective gating variables n, m and h. The parameters were taken from Hodgkin and Huxley's paper from 1952 (28), where the membrane potential is shifted so that the resting potential is at 0 mV (25, 28). At 40 ms a pulse of $I_{\text{ext}} = 3$ μA/cm^2 is applied to the neuron, and due to the low amplitude of the current no action potential is generated. Later, for $I_{\text{ext}} = 8$ μA/cm^2, an action potential is produced, although, a reapplication of the current right after the firing does not trigger a new action potential due to the hyperpolarization phase. The gating variables show how the channels work during the firing of action potentials. n represents the activation of the potassium voltage-gated channels, which open fast during an action potential, however, not as fast as the m variable that describes the activation of sodium channels. The inactivation of the sodium channels is represented by h, and after the action potential these channels become inactivated very fast. This inactivation is the reason why there are no generation of successive action potentials.

Table 2.3 associates the mathematical description with its biological counterpart. Despite the lack of knowledge about the mechanism of ion channels, Hodking and Huxley's proposal of the 4th and cubic power in n and m, respectively, elucidated a fundamental mechanism behind ion channels. They reached n^4 and m^3 through fitting experimental data. However, years later it was discovered that these powers are related to gates that compose ion channels (25). Four activation gates compose the potassium channels, three activation gates and one inactivation gate compose the sodium channels.

Figure 13 – (a) The current pulses applied to the neuron and the membrane potential V and (b) the respective gating variable n, m and h. We consider C = 1 pF, $g_{\mathrm{L}} = 12$ nS, $E_{\mathrm{L}} = 10.6$ mV, $E_{\mathrm{Na}} = 120$ mV, $E_{\mathrm{K}} = -12$ mV, $g_{\mathrm{Na}} = 120$ nS, $g_{\mathrm{K}} = 36$ nS and $g_{\mathrm{L}} = 0.3$ nS (28). Simulation time = 0.01 seconds.

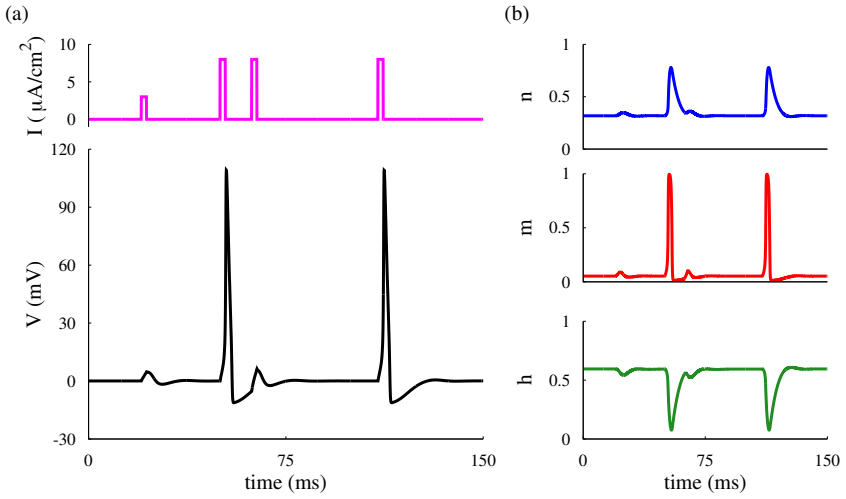

Source: the author

Table 2.3 – Equivalency of the mathematical description with the biological counterpart.

Mathematical description	Biophysical meaning
$g_{\mathrm{L}}, \overline{g}_{\mathrm{K}}, \overline{g}_{\mathrm{Na}}$	Conductance of the leaky, potassium and sodium channels.
$E_{\mathrm{L}}, E_{\mathrm{K}}, E_{\mathrm{Na}}$	Equilibrium potential of leaky, potassium and sodium ions.
n^4	Activation of potassium channels.
m^3	Activation of sodium channels.
h	Inactivation of sodium channels.
I_{ext}	External stimulus.
$g_{\mathrm{L}}(V - E_{\mathrm{L}})$	Leaky current across the membrane, ions flow through resting channels equilibrating the concentrations of the intra and extracellular regions, mostly Cl^-.
$\overline{g}_{\mathrm{K}} n^4 (V - E_{\mathrm{K}})$	Potassium current across the voltage-gated channels.
$\overline{g}_{\mathrm{Na}} m^3 h (V - E_{\mathrm{Na}})$	Sodium current across the voltage-gated channels.

Font: the author.

2.4.3 Adaptive exponential integrate-and-fire model (AEIF)

In 2005, Brette and Gerstner (33) proposed the adaptive exponential integrate-and-fire model (AEIF). This model is an improvement of the LIF model, where they consider an exponential term and an adaptive current to better describe the slow dynamics of potassium ions (33, 34). The exponential term describes the fast increase of the potential when the threshold potential is reached (33, 37). Due to these enhancements, the model reproduces different

activities observed in cortical neurons (34, 37, 70). The AEIF model consists of two differential equations: one describing the membrane potential V and the other representing the adaptive current w. They are written as

$$C\frac{dV}{dt} = -g_{\mathrm{L}}(V-E_{\mathrm{L}}) + g_{\mathrm{L}}\Delta_{\mathrm{T}}\exp\left(\frac{V-V_{\mathrm{T}}}{\Delta_{\mathrm{T}}}\right) - w + I, \tag{2.22}$$

$$\tau_w\frac{dw}{dt} = a(V-E_{\mathrm{L}}) - w, \tag{2.23}$$

where C is the capacitance, g_{L} is the leak conductance, Δ_{T} is the slope factor, V_{T} is the threshold potential, I is the injected current, τ_w is the adaptation time constant and a is the adaptation coupling parameter. These parameters have physiological meaning (33, 37), which we will discuss shortly, allowing the model to reproduce activity observed in real neurons (71–73). In the LIF model, a reset condition is applied to the neuron when the membrane potential surpasses a maximum value. The AEIF model has a similar mechanic of resetting the variables: when $V \geq V_{\mathrm{max}}$ one reset condition is applied to the membrane potential and another to the adaptive current

$$V \rightarrow V_{\mathrm{reset}}, \tag{2.24}$$

$$w \rightarrow w_{\mathrm{reset}} = w + b, \tag{2.25}$$

where V_{reset} is the reset value of the membrane potential and b is an increment in the adaptive current (33). The parameters considered in this work are displayed in table 2.4, unless stated otherwise.

Table 2.4 – Parameters used in the AEIF simulations in this work.

C	g_{L}	E_{L}	Δ_{T}	V_{T}	τ_w	a	V_{max}
200 pF	12 nS	-70 mV	2 mV	-50 mV	300 ms	2 nS	-40 mV

Font: BRETTE, R.; GERSTNER, W. Adaptive exponential integrate-and-fire model as an effective description of neuronal activity. Journal of Neurophysiology, v. 94, n. 5, p. 3637–3642, 2005.

The AEIF model describes different mechanisms involved in the generation of action potentials. The term $g_{\mathrm{L}}(V-E_{\mathrm{L}})$ represents the leak current, taking the neuron to its rest potential E_{L}, which is associated with the flow of ions through resting channels. To faithfully describe the activation of an action potential, Brette and Gerstner (33) added an exponential function $g_{\mathrm{L}}\Delta_{\mathrm{T}}\exp((V-V_{\mathrm{T}})/\Delta_{\mathrm{T}})$. This term approximately describes the fast activation of the sodium channels during the depolarization process (33, 37). For $V > V_{\mathrm{T}}$, the exponential term assumes high values reproducing the fast flow of sodium to the inside of the neuron. The adaptive current w directly affects the neuronal potential since it describes the slow dynamics of some ion channels (37), for instance, the potassium channel. The adaptive time constant τ_w and the adaptation coupling parameter a are related to the slow channel. τ_w is the same time

constant that is measured of a channel and a is the sensitivity of the channel to a change in the membrane potential. To induce action potentials firing in the model, a depolarizing current I is applied to the neuron. The description of the terms of the model is summarized in the table 2.5.

Table 2.5 – Equivalency of the mathematical description with the biological counterpart.

Mathematical description	Biophysical meaning
$g_{\mathrm{L}}(V - E_{\mathrm{L}})$	Leaky current across the membrane, ions flow through resting channels.
$g_{\mathrm{L}}\Delta_{\mathrm{T}} \exp\left(\frac{V - V_{\mathrm{T}}}{\Delta_{\mathrm{T}}}\right)$	Fast activation fo sodium channels during depolarization.
w	Slow dynamics of specific ion channels for instance potassium channels.

Source: the author.

One of the most important and essential information about neurons is their firing frequency denoted by F (1, 33, 37). The firing frequency of a neuron can be calculated by determining the time between two successive action potentials. This time interval is called interspike-intervals (ISI), see Figure 14. The ISI of two spiking is $\mathrm{ISI}_n = t_{n+1} - t_n$, where t_n is the nth spiking of the neuron after a transient time interval (34). The mean ISI is defined as

$$\overline{\mathrm{ISI}} = \frac{1}{n_{\mathrm{final}} - n_{\mathrm{initial}} - 1} \sum_{n=n_{\mathrm{initial}}}^{n_{\mathrm{final}}} \mathrm{ISI}_n, \tag{2.26}$$

where n_{final} is the last spiking of the simulation, n_{initial} is the first action potential after the transient interval. The frequency rate is the inverse of the mean ISI, $\mathrm{F} = \overline{\mathrm{ISI}}^{-1}$. The F-I diagram

Figure 14 – Representation of the spike time t_n and the ISI. We consider $I = 500$ pA, $V_{\mathrm{reset}} = -68$ mV and $b = 60$ pA.

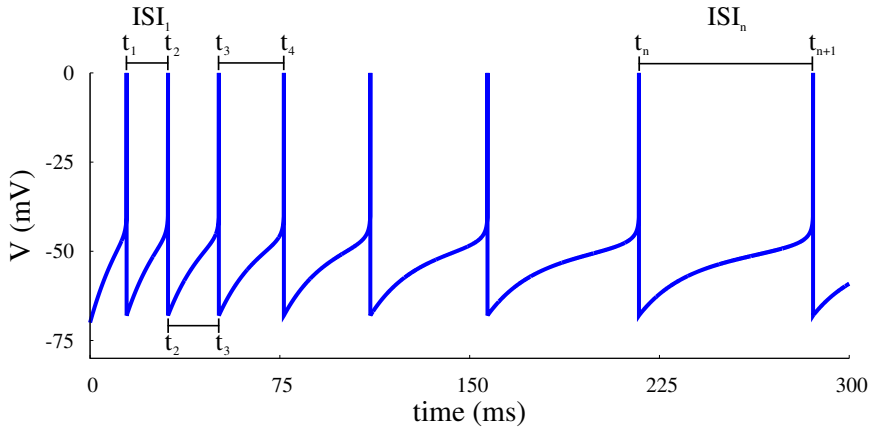

Source: the author.

is a well-known method used in neuroscience to understand the relationship between an applied current and the frequency produced in the neuron (37, 74). This diagram is also employed

to study the influence of the current in the neuronal models (74). Figure 15 displays the F-I relation for the AEIF model. The different symbols and colors represent the different frequency bands δ frequency (0.5 — 4 Hz) in blue square, θ frequency (4 — 8 Hz) in magenta hexagon, α frequency (8 — 13 Hz) in brown circles, β frequency (13 — 35 Hz) in yellow diamonds, and γ frequency (35+ Hz) in red triangles. These frequency bands are related to some cognitive tasks (75). The frequency increases linearly with the current amplitude for $I > 225$ pA whereas for lower values no spiking is observed. The minimum current necessary for the generation of an action potential is called rheobase current (1, 34, 37). The rheobase current in the AEIF model is given by Equation (2.28) if $a/g_{\mathrm{L}} > C/(g_{\mathrm{L}}\tau_w)$ and by Equation (2.28) if $a/g_{\mathrm{L}} < C/(g_{\mathrm{L}}\tau_w)$ (34)

$$I_{\mathrm{rheo}} = (g_{\mathrm{L}}+a)\left[V_{\mathrm{T}}-E_{\mathrm{L}}-\Delta_{\mathrm{T}}+\Delta_{\mathrm{T}}\ln\left(1+\frac{\tau_{\mathrm{m}}}{\tau_w}\right)\right]+\Delta_{\mathrm{T}}g_{\mathrm{L}}\left(\frac{a}{g_{\mathrm{L}}}-\frac{\tau_{\mathrm{m}}}{\tau_w}\right), \quad (2.27)$$

$$I_{\mathrm{rheo}} = (g_{\mathrm{L}}+a)\left[V_{\mathrm{T}}-E_{\mathrm{L}}-\Delta_{\mathrm{T}}+\Delta_{\mathrm{T}}\ln\left(1+\frac{a}{g_{\mathrm{L}}}\right)\right]. \quad (2.28)$$

Figure 15 – F-I diagram of the AEIF model. We consider $I = 500$ pA, $V_{\mathrm{reset}} = -68$ mV and $b = 60$ pA. Simulation time = 0.013s

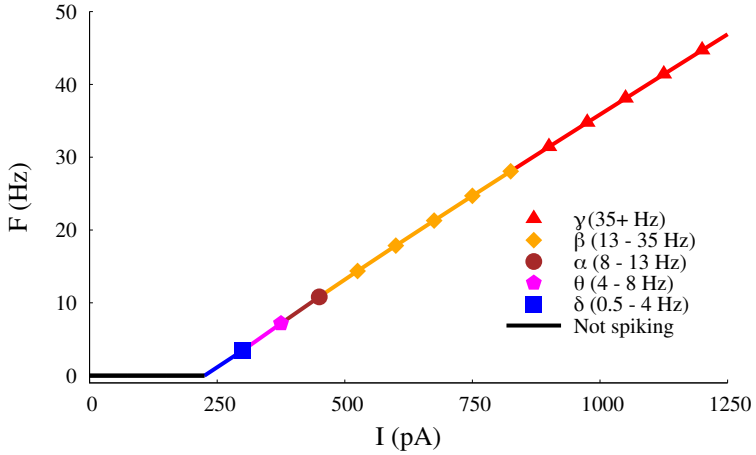

Font: the author.

The AEIF model is capable of reproducing different firing patterns from adaptive spiking to irregular bursting. Different combinations of the reset parameters (V_{reset}, b) produce this variety of patterns (33, 34). Figure 16 displays the five patterns which the AEIF model reproduces: adaptation spike ($V_{\mathrm{reset}} = -68$ mV, $b = 60$ pA), tonic spike ($V_{\mathrm{reset}} = -65$ mV, $b = 5$ pA), initial burst ($V_{\mathrm{reset}} = -48.8$ mV, $b = 35$ pA), regular burst ($V_{\mathrm{reset}} = -47.4$ mV, $b = 41$ pA) and irregular burst ($V_{\mathrm{reset}} = -47.4$ mV, $b = 41.2$ pA). To identify these distinct firing patterns is necessary to calculate the coefficient of variation (CV), and the adaptation index (A) and to analyze the reset regions of V and w in the phase plane (34, 37).

In this work, we focus our analysis on the coefficient of variation (CV) that identifies

Figure 16 – Firing patterns of the AEIF model, these patterns are obtained by different combinations of the reset parameters. We consider $I = 500$ pA. Simulation time = 0.011 s.

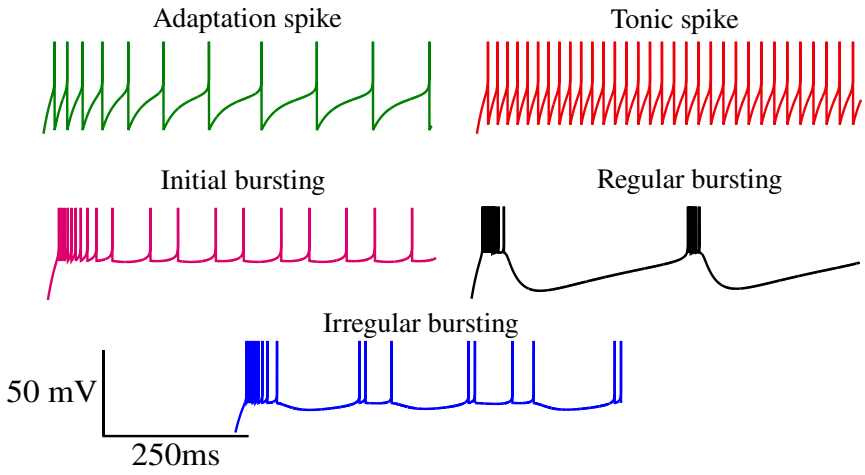

Font: the author.

spike and burst activity. Spikes are patterns of isolated action potentials followed by a period of silence where the neuron does not fire, for instance, the adaptive spiking in Figure 16. Meanwhile, burst activity is a pattern of clustered spikes followed by a long period in which the neuron does not produce action potentials, for example, the regular bursting in Figure 16. Neurons can exhibit spiking or bursting activity during the application of a stimulus. Analyzing the time series of the membrane potential makes it possible to identify each. The coefficient of variation (CV) is a statistical tool that enables us to quantitively distinguish both patterns. The CV is defined as

$$\mathrm{CV} = \frac{\sigma_{\mathrm{ISI}}}{\overline{\mathrm{ISI}}}, \tag{2.29}$$

where σ_{ISI} is the standard deviation of ISIs and $\overline{\mathrm{ISI}}$ is the mean ISI (13, 34, 35). This tool analyzes the variability of the interspike intervals, and it is able to detect spiking and bursting due to the great variability of the ISIs in the bursting pattern. Spiking and bursting activity produce distinct values of CV. A neuron in a spiking pattern yields $\mathrm{CV} < 0.5$, whereas bursting activity yields $\mathrm{CV} \geq 0.5$. (13, 34, 35). Figure 17 displays the reset parameters combinations that produce spike or burst in the model. In region I only spikes are produced ($\mathrm{CV} < 0.5$) and bursts are observed in region II ($\mathrm{CV} \geq 0.5$). The model generates a burst activity for values of V_{reset} closer to the V_{max}. To analyze the firing patterns of a single neuron, we consider a transient time of $t_{\mathrm{inital}} = 1$ s and the end of simulation $t_{\mathrm{final}} = 5$ s.

The Hodgkin-Huxley and AEIF models are two of the most commonly used models for describing the electrical activity of a neuron or populations of neurons (14, 16, 35, 37). For instance, to describe more precisely the activity of human neurons some adaptation must be done in the Hodking-Huxley model since this model lacks the dynamics of certain ionic channels such as calcium and slow potassium (16, 76). Borges et al. (16) have modeled a random network of spike neurons considering the calcium and slow potassium ionic currents. They have

Figure 17 – Region I (beige color) represents the spike activity and region II (red color) the burst behavior. We consider $I = 500$ pA. Simulation time = 5 minutes and 3.392 seconds.

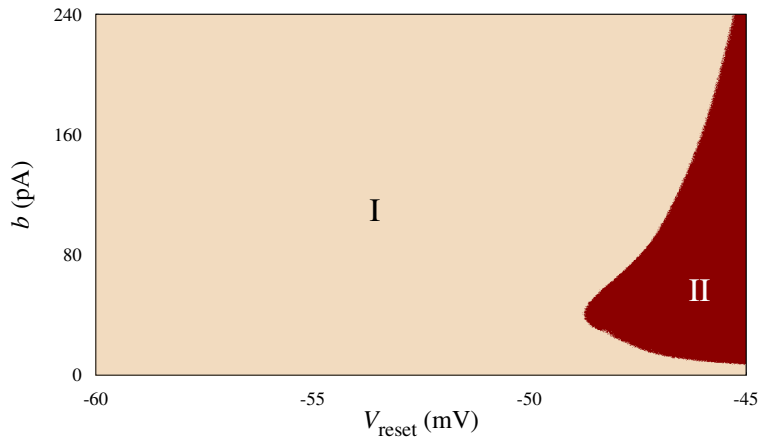

Font: the author.

shown that in the presence of slow potassium dynamics, the neurons are capable of producing bursting activity which is not observed in the original Hodgkin-Huxley model. Furthermore, they have demonstrated that calcium channels attenuate the emergence of synchronous bistable states. The AEIF model has been extensively applied for the study of multiple brain activities (12–14, 35, 37, 71, 72). For instance, Souza et al. (12) have shown that this model is capable of reproducing multiple wave patterns experimentally observed in the brain. Protachevicz et al. (13) demonstrated that bistable states can be modeled by a population of AEIF neurons. They theorized that such activity is linked with the slow dynamics of the adaptive current variable. In the following chapter, we introduce the network model of an excitatory layer of the hippocampus and the diagnostic tools that we consider in this dissertation.

3 METHOD AND ANALYSIS TOOLS

In this chapter, we present the network of adaptive exponential integrate-and-fire neurons considered in this work. The analysis tools we consider are the coefficient of variation (CV) and the Kuramoto order parameters. The CV was presented in the previous chapter and is discussed in more detail in subsection 3.2.1. The Kuramoto order parameters are statistical tools that measure the synchronization degree of coupled elements. The global order parameter determines the synchronization of the entire network, while the local order parameter measures the synchronization of nearby elements.

3.1 NEURONAL NETWORK MODEL

To describe a network composed of N AEIF neurons, we have to modify the equation 2.23 presented for a single neuron. The model lacks the synaptic input that a neuron i receives and sends. Therefore, we add a term to describe the synaptic current (I_i^{syn}). The following equations describe a network composed of excitatory AEIF neurons connected by chemical synapses

$$C\frac{dV_i}{dt} = -g_{\text{L}}(V_i - E_{\text{L}}) + g_{\text{L}}\Delta_{\text{T}}\exp\left(\frac{V_i - V_{\text{T}}}{\Delta_{\text{T}}}\right) - w_i + I + \underbrace{\sum_{j=1}^{N}(V_{\text{rev}}^j - V_i)M_{ji}g_j}_{I_i^{\text{syn}}}, \quad (3.1)$$

$$\tau_w\frac{dw_i}{dt} = a(V_i - E_{\text{L}}) - w_i, \quad (3.2)$$

$$\tau_g\frac{dg_i}{dt} = -g_i, \quad (3.3)$$

where V_i, w_i and g_i describe the potential, adaptative current, and the synaptic conductance, respectively, of the ith neuron. The synaptic current term $I_i^{\text{syn}} = \sum_{j=1}^{N}(V_{\text{rev}}^j - V_i)M_{ji}g_j$ describes the chemical synapses that arrive at neuron i, where V_{rev}^j is the reverse potential of the j-neuron, M_{ji} is the adjacency matrix ($M_{ji} = 0$ if j-neuron is not connected with i-neuron and $M_{ji} = 1$ otherwise) and the g_j is the synaptic conductance. The reverse potential V_{rev}^j is $V_{\text{rev}}^j = 0$ mV for excitatory neurons. This value is associated with the positive flux of current to the post-synaptic neuron after receiving the excitatory chemical synapses. In a single-cell model, two reset parameters are necessary to describe the model when $V_i \geq V_{\max}$. However, in a network, one more reset condition is necessary $g_i \to g_i + g_{\text{syn}}$, where g_{syn} is the coupling strength between two neurons. When the j-neuron fires $V_j > V_{\max}$ this reset condition is applied to the i-th neurons synaptic conductance. To simulate the network, we consider the parameters presented in Table 2.4, with the fixed reset parameters $V_{\text{reset}} = -58$ mV and $b = 70$ pA. A constant current is applied to each neuron $I = 500$ pA. To avoid any transient effect and to ensure the stability of the firing patterns, we consider the final 5 seconds of the 30-second simulation.

The neurons in our network are organized following the spatial distribution of the hippocam-

pus CA1 region, which was demonstrated by Bezaire et al. (38, 39) in 2016. They showed that the CA1 of a rodent can be represented as the combination of ten neuron layers where different morphological neurons compose each layer. In their work, the authors construct a biophysical network composed of 9 types of morphological neurons, each with its specific shape, connectivity and functionality (39). However, since we consider punctual neurons in this work, we simplify these nine types into their synaptic output type, excitatory or inhibitory. Figure 18 displays a simplified representation of Bezaire's network (considering that the neurons are either excitatory or inhibitory), where the blueish rectangles represent the inhibitory layers, the reddish rectangles illustrate the excitatory layers and the z position of each layer are depicted as well. Most layers have only one type of neuron, excitatory or inhibitory, although, there is one layer, located at $z = 125$ µm, where both neurons are present. The information regarding the spatial distribution of each neuron type in Bezaire's network is displayed in Table 3.1 to avoid confusion about each neuron type name we denominate them as T1, T2, T3, ..., T9.

Most excitatory neurons in the hippocampus possess long axons which enable their connections with inhibitory neurons in far layers and with different regions of the hippocampus (39, 77). However, in our network, the neurons are single-compartment[1] models and lacks the morphology for the long-distance coupling of excitatory and inhibitory neurons. Therefore, we consider a single excitatory layer at $z = 105$ μm and investigate the dynamics that emerge in such a bidirectional network. Since we consider one excitatory layer, we represent the coupling between neurons as local connections maintaining some biophysical accuracy. We consider a 1000×1000 μm layer which is composed of $17,324$ neurons. The superficial neuronal density in our model is measured in the CA1 region (38, 78, 79). Figure 19 displays a representation of the spatial distribution of the layer considered in this dissertation.

Table 3.1 – Spatial distribution of each neuron type (T1, T2, ..., T9). Where x_0, y_0, and z_0 represent the position of the first neuron of each type, δ_x, δ_y, and δ_z are the (x, y, z) distance of two similar neurons.

	Excitatory	Inhibitory							
	T1	T2	T3	T4	T5	T6	T7	T8	T9
x_0 (μm)	3.5	19.5	19.5	14.0	7.5	10.5	25.5	34.0	22.0
δ_x (μm)	7.0	38.0	39.0	28.0	15.0	21.0	51.0	68.0	44.0
y_0 (μm)	4.0	26.0	31.0	19.0	14.0	26.0	31.0	71.0	25.0
δ_y (μm)	8.0	62	45.0	38.0	28.0	33.0	52.0	142.0	50.0
z_0 (μm)	105.0	50.0	125.0	125.0	125.0	125.0	125.0	250.0	375.0
δ_z (μm)	10.0	none	none	none	none	none	none	none	50
Nº layers	5	1	1	1	1	1	1	1	2
Nº neurons	311,500	1640	2210	3600	8810	5530	1470	400	3580

Source: the authors.

In our network, the neurons only establish local connections with other neurons inside a radius R. Let us consider one layer and two neurons that compose it, with the ith neuron located

[1]The entire neuron is represented by a unique compartment, there are no dendrites nor axons, only the soma.

Figure 18 – Representation of the Bezaire's network (39).

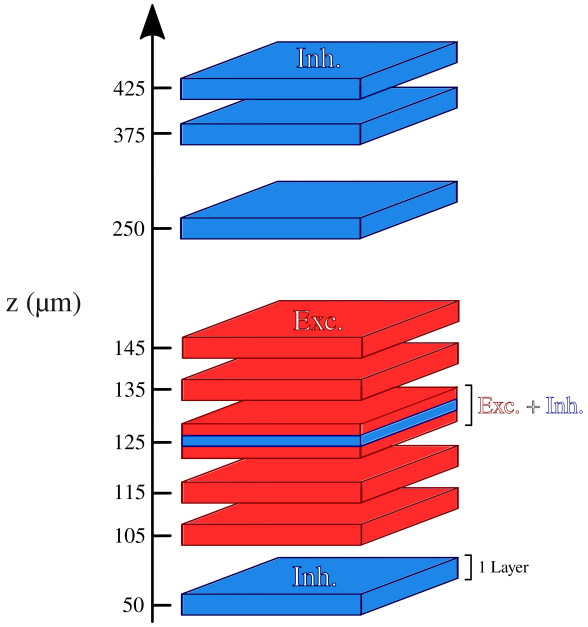

Source: the author

at (x_i, y_i) and a jth neuron located at (x_j, y_j). The Euclidean distance D between them is given by

$$D = \sqrt{(x_j - x_i)^2 + (y_j - y_i)^2}. \tag{3.4}$$

For i to connect with j, we define an arbitrary radius of connection R such that $D \leq R$ both neurons are connected and $M_{ij} = 1$, otherwise $M_{ij} = 0$. The Figure 19 displays an illustration of the connection of a neuron given a radius R.

Figure 19 – Connection representation between neurons within an arbitrary radius R. The xy distance between each neuron is represented in the bottom right.

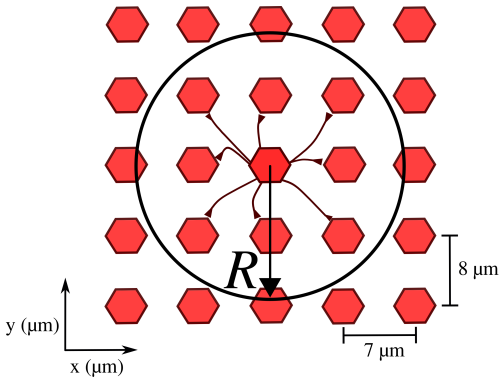

Source: the author.

3.2 ANALYSIS TOOLS

In this section, the firing pattern and synchronization analysis tools are introduced. The coefficient of variation (CV) for a single neuron was briefly discussed in the previous chapter, now the CV is extended to evaluate the firing pattern of a network composed of N neurons. The interaction among multiple elements in a network gives rise to many interesting phenomena such as resonance, phase locking, synchronization, and others (15, 80). We focus our study on the local and global synchronization of the neurons. To quantitatively measure the synchronization of the network, we employ the local and global Kuramoto order parameter (40, 41). Firstly, we describe the CV for a network and then, we present and discuss both glocal and local Kuramoto order parameters.

3.2.1 Coefficient of variation

The coefficient of variation is a statistical tool that measures the dispersion of the interspike interval (ISI) distribution. In order to calculate the CV, first is necessary to determine the mean interspike interval of each neuron ($\overline{\text{ISI}}_i$), defined as

$$\overline{\text{ISI}}_i = \frac{1}{n_i^{\text{final}} - n_i^{\text{initial}} - 1} \sum_{n=n_i^{\text{initial}}}^{n_i^{\text{final}}} \text{ISI}_{i,n}, \tag{3.5}$$

where n_i^{final} is the last firing of the ith neuron, n_i^{initial} is the first firing of ith neuron after a transient time, and $\text{ISI}_{i,n}$ is the interspike interval of the nth firing ($\text{ISI}_{i,n} = t_{i,n} - t_{i,n-1}$). Note that Figure 14 displays the ISI of a single neuron. Given the mean interspike interval of each neuron, it is possible to calculate the standard deviation σ_{ISI_i} (34)

$$\sigma_{\text{ISI}_i} = \sqrt{\frac{1}{n_i^{\text{final}} - n_i^{\text{initial}} - 1} \sum_{n=n_i^{\text{initial}}}^{n_i^{\text{final}}} (\text{ISI}_{i,n} - \overline{\text{ISI}}_i)^2}. \tag{3.6}$$

Thus, it is possible to determine the coefficient of variation of the ith neuron

$$\text{CV}_i = \frac{\sigma_{\text{ISI}_i}}{\overline{\text{ISI}}_i}, \tag{3.7}$$

with the mean coefficient of variation $\overline{\text{CV}}$ given by

$$\overline{\text{CV}} = \frac{1}{N} \sum_{i=1}^{N} \text{CV}_i. \tag{3.8}$$

In this work, we employ the mean coefficient of variation to analyze whether the network is in a spike or burst firing pattern since noth firing patterns produce characteristic values for $\overline{\text{CV}}$. If $\overline{\text{CV}} < 0.5$, the network is presenting a spike pattern, and for $\overline{\text{CV}} \geq 0.5$, burst activity

is displayed by the network (13, 34). Figure 20 displays the membrane potential and the ISI distribution for an arbitrary neuron considering two values of g_{syn}, namely, (a) $g_{syn} = 0.05$ nS and (b) $g_{syn} = 0.15$ nS. With coupling $g_{syn} = 0.05$ nS, the neuron exhibits spike activity and we obtain a single value for its ISI. for a more intense coupling the neuron presents burst activity and more possibilities of ISI_i values.

Figure 20 – Example of the membrane potential and the ISI distribution for (a) spike ($g_{syn} = 0.05$ nS) and (b) burst ($g_{syn} = 0.15$ nS) activities. We consider the parameters presented in table 2.4 and $R = 70$ μm. Simulation time = 2 minutes 37 seconds, cores = 2.

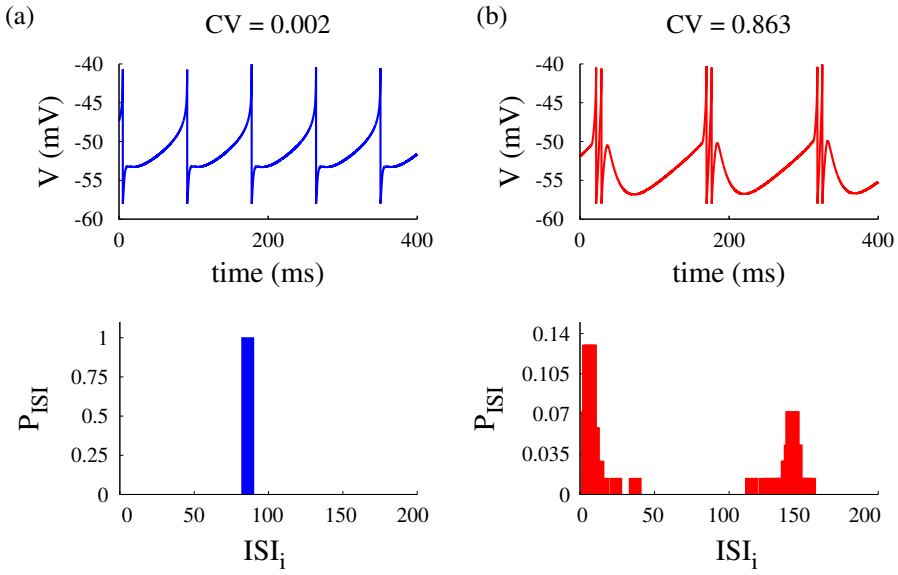

Source: the author.

3.2.2 Global Kuramoto order parameter

The global Kuramoto order parameter is a mathematical tool that estimates the synchronization degree of all elements in a network (41). Before calculating the Kuramoto order parameter, we must transform the elements of the network into a phase oscillator (41) with phase $\varphi_i(t)$. The phase of a neuron i is defined as

$$\varphi_i(t) = 2\pi m + 2\pi \frac{t - t_{i,m}}{t_{i,m+1} - t_{i,m}}, \tag{3.9}$$

where m is the m-th firing of the neuron i and $t_{i,m}$ is the time instant of the m-th firing of the neuron i with t restricted to the interval $t_{i,m} \leq t \leq t_{i,m+1}$. The intervals of t update at each firing of the neuron i. Figure 21 displays the representation of the phase of a neuron i. When the neuron produces an action potential, the phase assumes the values 0 or 2π and while the neuron is in silence (not firing) the phase assumes values between 0 and 2π.

After describing the phase $\varphi_i(t)$ of each neuron it is possible to define the global Kuramoto

Figure 21 – Representaion of the phase $\varphi_i(t)$ between spikes of a neuron i throughout the time.

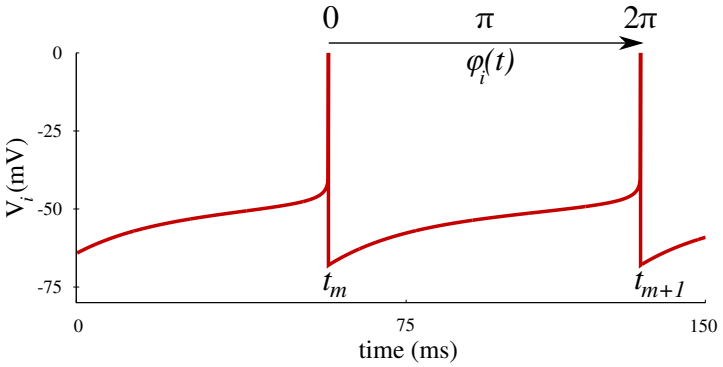

order parameter Z(t) as

$$\mathrm{Z}(t) = \frac{1}{N}\left|\sum_{j=1}^{N} \exp\left(i\varphi_j(t)\right)\right|. \tag{3.10}$$

The maximum value that Z(t) can assume is 1, meaning that the network is totally synchronized, and all neurons are firing simultaneously. Meanwhile, the lowest value that Z (t) can reach is 0 which points to total desynchronization. For $0 < Z(t) < 1$ partial synchronization is observed. The mean value $\overline{\mathrm{Z}}$ yields the information of the synchronization during the time evolution, differently from Z (t) which only points to synchronization and desynchronization in a specific instant of time. The mean global Kuramoto order parameter Z_g is

$$\mathrm{Z}_g = \frac{1}{t_{\text{final}} - t_{\text{initial}}} \int_{t_{\text{initial}}}^{t_{\text{final}}} \mathrm{Z}(t)dt, \tag{3.11}$$

where t_{initial} and t_{final} mark the beginning and ending, respectively, of the time window under analysis. If the network displays synchronous activity, Z_g is approximately 1. Otherwise, it approaches 0. Figure 22 display Z(t) and the raster plot for two combinations of g_{syn} and R. In panels (a) and (c) ($g_{\text{syn}} = 0.01nS$ and $R = 20\ \mu$m), the global Kuramoto order parameter is around 0.194 and $\mathrm{Z}_g = 0.202$ which is characterized as asynchronous activity. The raster plot for this case is displayed in panel (c), where the y-axis is the neuron index i, the x-axis is the time, and each point on it represents that the neuron i has fired an action potential. This graphic is an interesting visual tool for observing desynchronization and synchronization activity. When the network is desynchronized, the points in the raster plot are very scattered meanwhile during synchronous activity they form vertical lines. In panels (b) and (d) ($g_{\text{syn}} = 0.05$ nS, $R = 70$), we observe synchronous activity. The Z (t) is close to 1 ($\mathrm{Z}_g = 0.964$) and the raster plot (panel (d)) displays a vertical pattern, which means that each neuron is firing approximately at the same time.

Figure 22 – Global Kuramoto order parameter (Z (t)) (a-b) and the raster plot (c-d) for two combinations of g_{syn} and R. In panels (a) and (c) we consider ($g_{syn} = 0.01$ nS, $R = 20$ μm) and ($g_{syn} = 0.05$ nS, $R = 70$) in panels (b) and (d). Simulation time = 2 minutes 43 seconds, cores = 2.

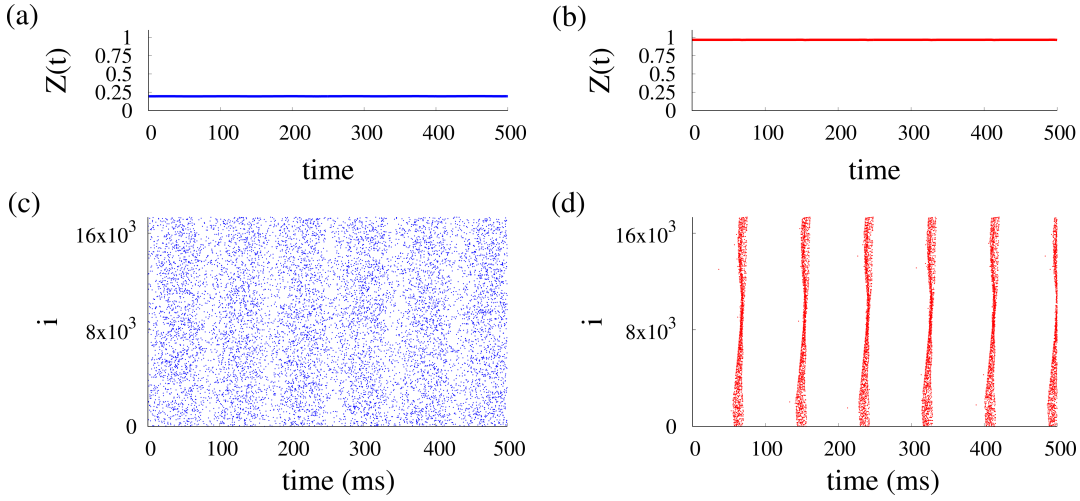

Font: the author.

3.2.3 Local Kuramoto order parameter

Differently from the global order parameter, the local order parameter depends on the spatial distribution of the neurons. It measures how locally synchronized are the neurons, identifying if neurons close to each other are firing simultaneously. To calculate the local Kuramoto order parameter, we divide our 1000×1000 μm network into smaller boxes of 40×40 µm. Where Figure 23 displays an illustration of the boxes. Each box is labeled by the index (l, m), similarly to matrix notation, where l means the "row" and m the "column". The maximum number of boxes in either direction is 25 and in total, we divide our network into 625 40×40 boxes to analyze the local synchronization. synchronization.

After separating the neurons into their respective boxes, the local Kuramoto order parameter of (l, m)-box is given by the sum of Euler's exponential of the phase of the j-neurons inside the (l, m)-box

$$Z_{l,m}(t) = \left| \frac{A^2}{N^2} \sum_{\substack{n=j \\ \in(l,m)}} \exp\left(i\varphi_j(t)\right) \right|, \tag{3.12}$$

where A is the total number of boxes ($A = 625$), N is the total number of neurons and j is the index of a neuron. To verify the local synchronization throughout the total simulation, we calculate the temporal mean of each (l, m)-box

$$\overline{Z}_{l,m} = \frac{1}{t_{\text{final}} - t_{\text{initial}}} \int_{t_{\text{initial}}}^{t_{\text{final}}} Z_{l,m}(t)dt, \tag{3.13}$$

where t_{initial} is the time instant of the start ($t_{\text{initial}} = 25$ s) of the analysis and t_{final} is the final time of the analysis ($t_{\text{final}} = 30$ s). Figure 24 displays the local Kuramoto order parameter of

Figure 23 – Representation of the (l,m)-boxes with some neurons within.

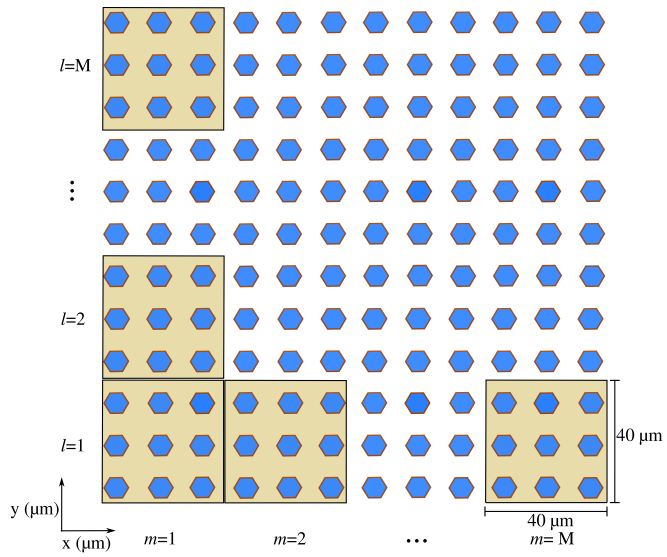

Source: the author.

each neuron for (a) ($R = 20\ \mu$m, $g_{\text{syn}} = 0.01$ nS) and (b) ($R = 70\ \mu$m, $g_{\text{syn}} = 0.05$ nS). The neurons are locally desynchronized in panel (a). Some neurons are more locally synchronized (blueish squares), however $\overline{Z}_{l,m}$ is not approximately 1, which cannot be characterized as local synchronization. In panel (b), on the other hand, we observe local synchronization of the neurons. To evaluate how locally synchronized is the entire network, we calculate the mean

Figure 24 – Mean local Kuramoto order parameter $\left(\overline{Z}_{l,m}\right)$ for (a) ($R = 20\ \mu$m, $g_{\text{syn}} = 0.01$ nS) and (b) ($R = 70\ \mu$m, $g_{\text{syn}} = 0.05$ nS). In the panel (a), we calculate $Z_L = 0.03$ which points that most neurons are locally desynchronized, and the panel (b) produces $Z_L = 0.98$. Simulation time = 2 minutes 53 seconds , core = 2.

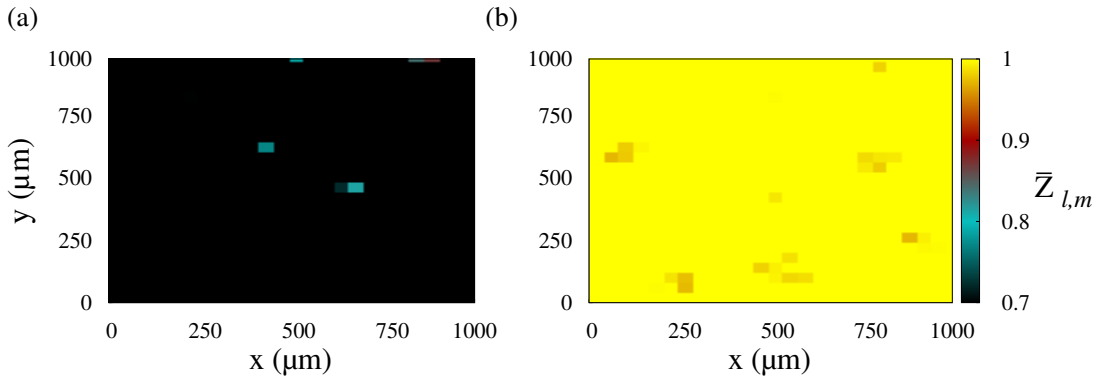

Source: the author.

local Kuramoto order parameter of all boxes

$$Z_L = \frac{1}{A}\sum_{l,m}^{25}\overline{Z}_{l,m}. \tag{3.14}$$

This measurement indicates if the network is locally synchronized ($Z_L \geq 0.7$) or locally desyn-

chronized ($Z_L \leq 0.7$).

3.3 SIMULATION METHODOLOGY

To numerically integrate all equations, we employ the 4th order Runge-Kutta with step $h = 0.05$ ms. All codes employed to solve and analyze the results are written in C-language and are available in a GitHub repository (81). The compiler used in this work is the Intel® one API DPC++/C++ Compiler (command icx). The simulations were run in the 105 science group's laboratory computer or the server of the Oscillations Control Group (INSTITUTE OF PHYSICS — UNIVERSITY OF SÃO PAULO). The computer setup is displayed in table 3.2. The details about simulation time and amount of cores used are displayed in the caption of each simulation. The initial conditions of V_i and w_i for each neuron are randomly chosen from predetermined ranges $V_i(0) \in [-70, -45]$ mV and $w_i(0) \in [0, 70]$ pA. We consider a random uniform generator. These initial conditions are kept the same for all simulations.

Table 3.2 – 105 science group's laboratory computer setup.

Processor	Intel® Core™ i9–9900K CPU @ 3.60GHzx16
Motherboard	MPG Z390 GAMING PLUS DDR4
RAM memory	2×8gb DDR4–3200Hz Kingston
SSD	480GB Kingston
Graphic card	Intel Corporation CoffeeLake-S GT2

4 ONE EXCITATORY HIPPOCAMPAL LAYER

In this chapter, we investigate the oscillations and synchronous dynamics that emerge in an excitatory hippocampal network of the CA1 region. In the first part, we evaluate the influence of the network parameters radius of connection (R) and coupling strength (g_{syn}) on the synchronization and firing pattern transition on a single excitatory layer composed of $N = 17,324$ neurons. The waves and the detection methodology of wave patterns are presented in the second section. In the last section of this chapter, we investigate the influence of the initial conditions on the wave patterns and the emergence of bistable regimes. The parameters of each neuron are displayed in Table 2.4, and the reset parameters considered are $V_{\text{reset}} = -58$ mV and $b = 70$ pA (spike region of Figure 17). We fix all the parameters of each neuron and focus our study on the detection of waves and synchronization due to the variation of the parameter's R and g_{syn}.

4.1 SYNCHRONIZATION AND FIRING PATTERN TRANSITION

In this section, we study the response of the neurons given different combinations of g_{syn} and R. Figure 25 (a-c) displays the membrane potential of (a) spike desynchronization $g_{\text{syn}} =$ 0.001 nS (blue circles), (b) spike synchronization $g_{\text{syn}} = 0.1$ nS (blue squares) and (c) bursting synchronization $g_{\text{syn}} = 0.2$ nS (blue triangles). Panel (d) shows Z_g (brown line) and Z_L (beige line) and (e) shows the coefficient of variation as a function of g_{syn}, with $R = 60$ μm.

The panels (a), (b) and (c) display the membrane potential for three values of coupling strength. Panel (a) shows spike desynchronization ($g_{\text{syn}} = 0.001$ nS) for three random neurons of the network and in this situation the neurons fire at distinct time instants. Panel (b) displays spike synchronization ($g_{\text{syn}} = 0.1$ nS) and panel (c) depicts burst synchronization ($g_{\text{syn}} = 0.2$ nS), in the burst activity CV≥ 0.5. In panel (d), we observe that the network is locally synchronized for most values of coupling strength, except for the case in which $g_{\text{syn}} < 0.007$ nS, a region where the neurons are locally and globally desynchronized ($Z_g < 0.5$ and $Z_L < 0.5$). This is related to the low interaction that each neuron has with its neighbors since the coupling in this case is low. For $g_{\text{syn}} > 0.2$ nS, the local synchronization presents values inferior to 1, although, this reduction yet yields local synchronization since $Z_L > 0.7$. This reduction is due to the transition from spike-to-burst that occurs at $g_{\text{syn}} > 0.2$ nS. There are ranges of g_{syn} in which the network is globally synchronized and others in which it is desynchronized. For $0.007 < g_{\text{syn}} < 0.12$ nS, the neurons are globally synchronized ($Z_g > 0.7$), while for greater values of coupling the neurons desynchronize. For $g_{\text{syn}} \geq 0.2$ nS the network synchronizes once more. These results show that global and local synchronization of the network depends on the couplings and that local synchronization does not depend on global synchronous activity, and vice versa. Panel (e) shows that as g_{syn} intensifies the network transition from spike to burst for $g_{\text{syn}} > 0.2$ nS. For $g_{\text{syn}} = 0.2$ nS the network displays synchronization of bursting, a pattern

which is associated with epileptic seizures (13, 14).

Figure 25 – The panels (a-c) exhibit the time evolution of the membrane potential V for three different values of g_{syn}. We observe (b) desynchronized spikes for $g_{syn} = 0.001$ nS (blue circle), (c) synchronized spike for $g_{syn} = 0.1$ nS (blue square), and (d) synchronized burst for $g_{syn} = 0.2$ nS (blue triangle). Panel (d) shows the global and local Kuramoto order parameter as a function of g_{syn} and panel (e) exhibits CV as a function of g_{syn}. We consider $R = 60$ μm. Simulation time = 37 minutes, cores = 10.

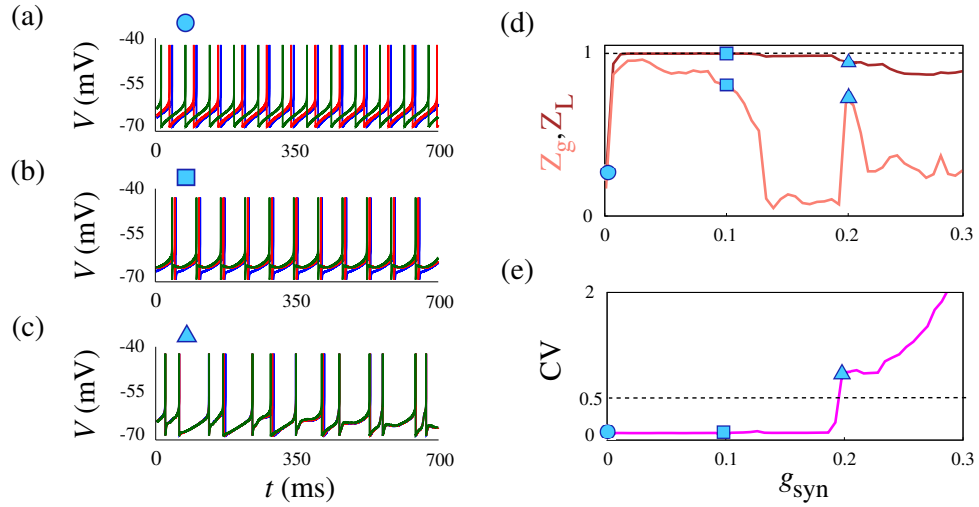

Source: the author.

Since the network displays four different firing patterns for different coupling strengths, now we investigate how R and g_{syn} affect the spike-to-burst transition and the synchronization. Figure 26 displays the $R \times g_{syn}$ parameter space of (a) Z_g, (b) Z_L, (c) CV and (d) F. Z_g parameter space is displayed in Figure 26 (a), which shows synchronous regions (bright color regions) and asynchronous areas (dark color regions). For $R < 20$, μm the network is globally desynchronized independently of g_{syn} due to the low mean degree connection of each neuron. For $R > 20$ μm, synchronous and asynchronous activity are observed for different combinations of R and g_{syn}. In the region $R > 50$ μm, the global synchronization depends on the coupling strength. Panel (b) displays the space parameter of Z_L, similarly with Z_g, the network does not locally synchronize for $R < 20$ μm. However, Z_L parameter space displays more synchronous regions compared with panel (a), this shows that achieving local synchronization is "easier" than global synchronization. The ranges for the coupling strength to reach local synchronization are vast. The CV is shown in panel (c), transitions from spike to burst are observable for $R > 50$ μm. For $R < 50$ μm, the network does not produce a burst firing pattern even for high values of coupling strength. This occurs since for low values of R, the neurons do not receive many inputs, meaning that the burst is not facilitated by the input of other neurons. However, as R increases, each neuron receives more synaptic signals influencing the generation of more action potentials. Panel (d) displays the frequency (F) parameter space. Similarly to CV parameter space (panel (c)), the frequency greatly increases for a high value of R. Panels (a) and (c) show that for some specific values of R and g_{syn}, the network presents bursting synchronization for $R > 50$ μm and $g_{syn} > 0.15$ nS. These results show that when the network is locally synchronized, it

does not imply that it is globally synchronized. In the next section, we investigate these regions to understand how all neurons are mostly locally synchronized even if they are not on a global scale.

Figure 26 – $R \times g_{\text{syn}}$ parameter space. The color code represents the values of (a) the global order parameter (Z_g), (b) the local order parameter (Z_L), (c) the mean coefficient of variation ($\overline{CV}$) of the neuronal inter-spike interval and (d) the mean firing rate (F). Simulation run on the Oscillations Control Group server, Simulation time = 52 hours 17 minutes, cores = 16.

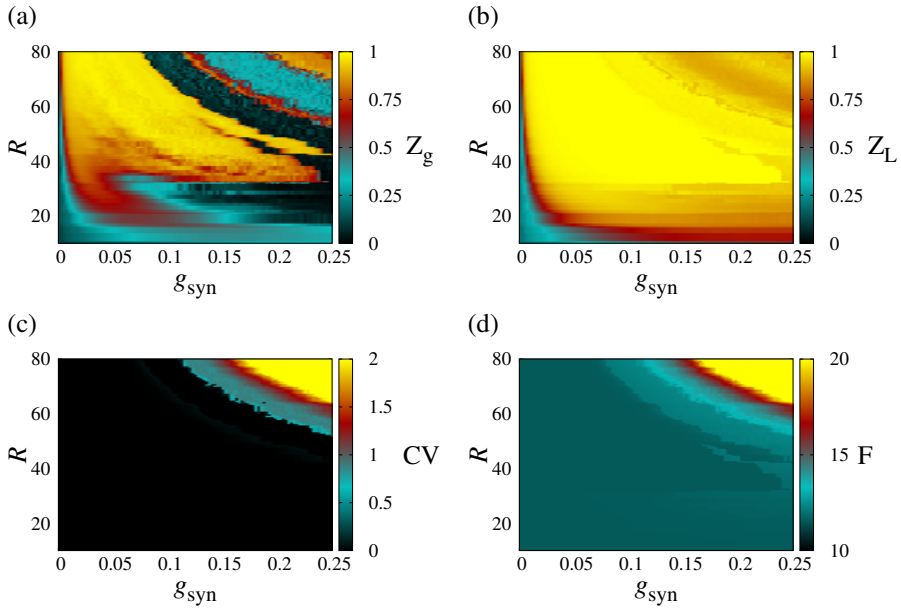

Source: the author.

4.2 WAVES AND SPIRAL DETECTIONS

Traveling waves are spatial-temporal patterns that propagate in 2D or 3D medium (82), and they have been observed in many scientific fields for instance neuroscience (8–10). In the brain, these waves are found in different brain regions such as the cortex and hippocampus (8). Their general function in the brain is not well understood until the moment. However, theta waves (6–12 Hz) detected in the CA1 hippocampus are related to the excitatory communication from small to large place cells[1] (8, 10) and some theta waves are also involved in the memory process (9).

Neuronal networks are able to reproduce such spatial-temporal patterns (8, 11). The visualization of the waves in a network can be done in two similar forms. One by plotting the membrane potential of each neuron and another by considering the neurons as phase oscillators and plotting the phase ($\varphi_i(t)$). In this work, we visualize the waves by plotting the phase of each neuron, where $0 < \varphi_i(t) < 2\pi$ represent that the neuron is silent[2] and $\varphi_i = [0; 2\pi]$ the

[1] Neurons that are specialized in processing spatial navigation information.

[2] The neuron is not spiking at this instant of time.

neuron is spiking. Figure 27 displays the phase of each neuron (panels (a), (c) and (e)) and the respective local order parameter ($\overline{Z}_{l,m}$) (panels (b), (d) and (f)) of each neuron for three different combinations of g_{syn} and R. Panel (a) displays the wave pattern for $g_{\text{syn}} = 0.15$ nS and $R = 32$ μm, which we denominate as multi-rings due to its shape. This pattern is related to asynchronous activity since each ring appears at a different time instant and propagates with similar velocity. The local Kuramoto order parameter of each neuron for the multi-ring pattern is displayed in panel (b). All neurons present high local synchronization since $Z_{l,m} \approx 1$, except for some darker spots ($0.95 < Z_{l,m} < 1$), these are the regions where each ring emerge. We measure $Z_g = 0.23$ and $Z_L = 0.99$. The synchronized rings phase is displayed in panel (c), $R = 55$ μm and $g_{\text{syn}} = 0.16$ nS. In this case, the rings emerge at the same time and propagate all together at the same speed. In this wave pattern, the local order parameter of each neuron is close to 1, however, there are some areas where $\overline{Z}_{l,m} < 0.95$ (reddish areas). Such regions are the core where each ring originates. The core of each ring in this case is in the reddish spots. The panels (e) and (f) are referent to the parameters $R = 75$ and μm $g_{\text{syn}} = 0.128$ nS, where burst synchronization is observed, with the phase displayed in (e) and $\overline{Z}_{l,m}$ in (f). The wave starts at one corner and propagates until the opposite side. This wave seems very long due to the high amount of action potentials that each neuron produces in a very short time during burst activity. Differently from other cases, when bursts appear in the network, border effects are seen in the $\overline{Z}_{l,m}$ plot.

Figure 27 – The upper panels (a), (c) and (e) display the phase ($\varphi_i(t)$) of each neuron, where the yellow color represents the fire of a neuron. Bottom panels (b), (d) and (f) exhibit the mean local Kuramoto order parameter ($\overline{Z}_{l,m}$) of each neuron for the multiring wave ($g_{\text{syn}} = 0.15$ nS and $R = 32$) (a), synchronized ring wave ($R = 55$ μm and $g_{\text{syn}} = 0.16$ nS) (c) and burst synchronization ($R = 75$ μm $g_{\text{syn}} = 0.128$) (e), respectively. Simulation time = 3 minutes 2 seconds, cores = 3.

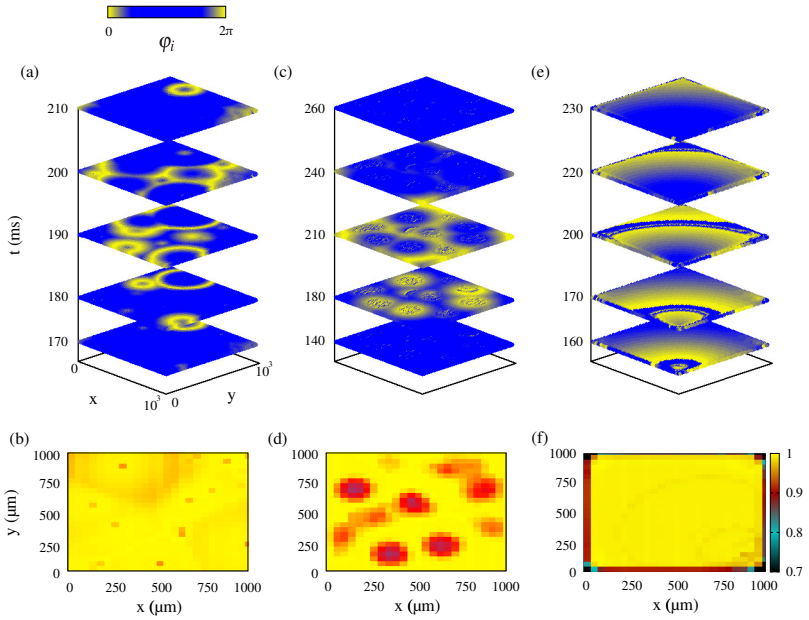

Source: the author.

Now we investigate different wave patterns that emerge. The network also displays chimera waves, where some neurons are synchronized and others are desynchronized simultaneously (83–87). Chimera states are defined as the coexistence of coherent and incoherent states at the same time (85), one type of chimera wave is the spiral wave. Spiral waves are astonishing chimera waves, where their core is composed of asynchronous elements (88) and they are denominated phase singularities (PS). This type of wave has been observed in different systems such as cardiac tissues (89) and neurons (12). Figure 28 displays three different chimera spiral waves, where panels (a), (c) and (e) show the phase and panels (b), (d) and (f) exhibit the respective $\overline{Z}_{l,m}$. Panel (a) displays a single spiral wave rotating around the phase singularity, we consider $R = 70$ μm and $g_{\text{syn}} = 0.12$ nS. $\overline{Z}_{l,m}$ of each neuron for the spiral wave is displayed in panel (b). Most of the neurons are synchronized, although, there is a darker region ($\overline{Z}_{l,m} \leq 0.7$) at $250 < x < 500$ and $500 < y < 750$ μm, where the center of the spiral is located. For $R = 75$ μm and $g_{\text{syn}} = 0.14$ nS, a spiral burst is obtained, and panel (c) displays the shape of this wave. Similarly, with the spike spiral wave, the helix of the spiral rotates around the phase singularity. This pattern produces CV$= 0.81$ which characterizes a burst, and another way of characterizing a burst spiral wave is by detecting silenced neurons (blue color) between two activated spirals (yellow color). The panel (d) displays $\overline{Z}_{l,m}$ of each neuron in the bursting spiral wave. A phase singularity is observed at the center of the spiral possessing $\overline{Z}_{l,m} < 0.7$, however, when burst activity is observed the borders of the network are not locally synchronized. We observe that any type of burst wave generates such patterns due to the high activity of the neurons. Therefore, we do not consider borders when analyzing the phase singularities. Panel (e) displays the phase of the coexistence of two different types of waves, multi-spirals and multi-rings. We denominate this type of wave as multi-spiral-ring, arising when $R = 30$ μm and $g_{\text{syn}} = 0.15$ nS. The $\overline{Z}_{l,m}$ is displayed in panel (f), and four black regions are observed. Each region represents a phase singularity (PS), and the pattern generated in panel (f) seems a combination of Figure 27 (b) and Figure 28 (a). The reddish regions around the PSs are due to the interaction of the spiral wave

The value of the mean global and local order parameter as well as the frequency of each wave pattern previously present in Figures 27 and 28 are exhibit in Figure 29, (a) Z_g in red and Z_L in blue and (b) frequency. The mean local order parameter of the different wave patterns displays a high local synchronization $Z_L \approx 1$, panel (a). This occurs for all types of waves due to the local dynamics that neuronal waves possess that close neurons fire together to create the spatial-temporal pattern. Meanwhile, the mean global order parameter Z_g of the waves is close to 0, which characterizes a global desynchronization, except for synchronous rings and synchronous bursts. These two wave patterns display waves even though their global synchronization is high. The frequency of each pattern is displayed in panel (b), most of the patterns possess very similar firing frequency F$\approx$ 12 Hz, excluding the synchronous burst and spiral burst which display F$\approx$ 14 Hz.

We observe that the traveling waves in our network present two main characteristics re-

Figure 28 – The upper panels (a), (c) and (e) display the phase ($\varphi_i(t)$) of each neuron, where the yellow color represents the fire of a neuron. Bottom panels (b), (d) and (f) exhibit the mean local Kuramoto order parameter ($\overline{Z}_{l,m}$) of each neuron for the spiral wave (a), burst spiral wave (c) and multi-spiral-rings (e), respectively. Simulation time = 2 minutes 57 seconds, cores = 3.

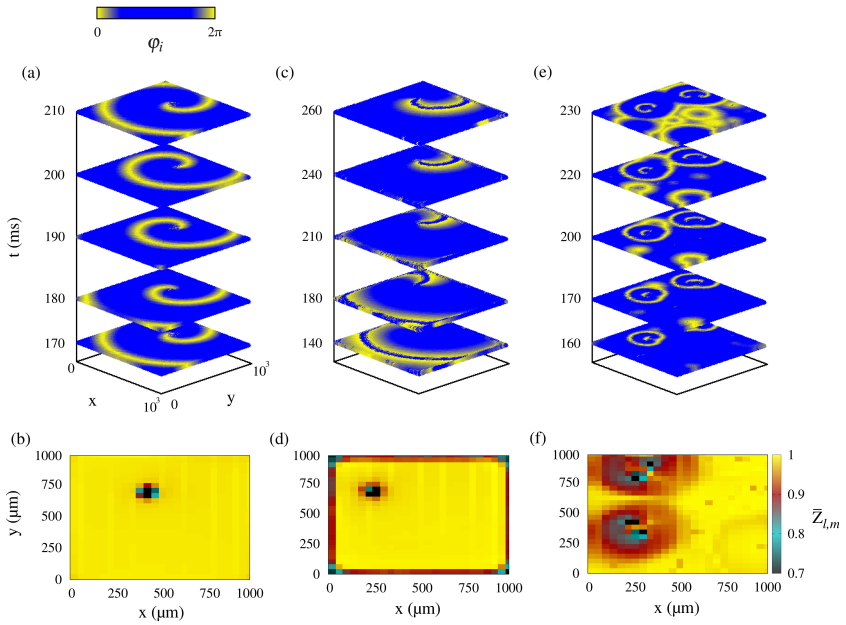

Source: the author.

Figure 29 – Diagnostic tools for the wave patterns presented in Figures 27 and 28. (a) displays the mean global order parameter Z_g in blue and the local order parameter Z_L in red, (b) shows the frequency rate F for each wave pattern.

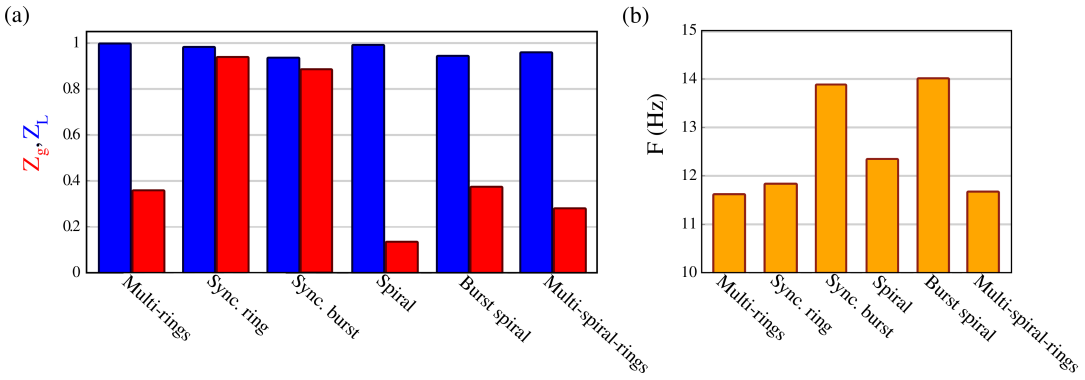

Source: the author.

garding the synchronization tools. All waves possess a very high mean local synchronization and a low global synchronization (except synchronization wave patterns). The global synchronization, excluding the synchronization wave patterns, is low which relates to the intense local activity of the neurons during a wave. Therefore, we propose a simple recipe for detecting the presence of a wave in the neuronal network

1. The mean local order Kuramoto Z_L of the time window analyzed must be close to 1, otherwise, the neurons are desynchronized and do not display a wave spatial pattern.

2. The mean global order Kuramoto parameter only holds the information regarding the global synchronization of the network. $Z_g \approx 1$ or $Z_g \approx 0$ does not yield any information regarding the presence of a wave in the network.

These conditions are enough for detecting a wave, however for characterizing them more information about the network is necessary. Now, we focus on a method capable of distinct spiral waves from non-spiral waves (for instance synchronous and multi-rings). The network displays a vast quantity of wave patterns. However, we focus on the spiral waves due to the lack of simple and reliable methods capable of detecting spiral waves in neuronal systems and also due to the fact that the emergence of spiral waves in neuronal networks is not well understood. Since our model is capable of producing a vast diversity of wave patterns we develop a method for identifying spiral waves based on the Kuramoto order parameter. Differently from other wave patterns presented in Figure 27, the spiral waves produce a local desynchronized characteristic pattern where the spiral is centered. The spiral waves rotate around a phase singularity that is composed of locally desynchronized neurons. Also, we observe that such cores must be well desynchronized meaning that the $\overline{Z}_{l,m}$ of the neurons located in the PS must be lesser than 0.7. There are combinations of (R, g_{syn}) where some neurons are locally desynchronized as displayed in Figure 27 (d). There are some neurons in which the local order parameter is close to 0.7, however, no spiral wave is observed. Therefore, we propose that for a spiral wave to appear in our network, some neurons must achieve some sort of "desynchronized threshold" which we set $\overline{Z}_{l,m} < 0.7$. Defining a local desynchronization threshold enables us to distinguish spiral waves from other wave patterns since no other wave pattern produces a high local desynchronization. Multi-spiral waves can be observed, however, as the number of PS increases the network starts to display local and global desynchronization. This behavior occurs due to the fact that each PS is a type of desynchronized cluster of neurons and as the number of PS increases more neurons display local desynchronization and $Z_L << 1$. Thus, we define the maximum number of PS that the network supports without total desynchronization. We present the following recipe for detecting a spiral wave

1. The emergence of a spiral wave in the network is related to the presence of local desynchronized neurons denominated as phase singularities PS, which produce $\overline{Z}_{l,m} < 0.7$. Otherwise, spiral waves are not observable in the network.

2. There is a maximum number of PS_{max} which the network can display simultaneously without displaying a total desynchronized pattern. We set $\text{PS}_{\text{max}} = 20$.

Figure 30 displays (a) the Z_g and (b) the number of phase singularities (PS) as a function of g_{syn} for $R = 75$ μm. The color scale displays the type of wave observed blue color represents desynchronization ($Z_g \approx Z_L \approx 0$ and PS> 20), red color displays synchronized wave patterns ($Z_g > 0.75$ and $Z_L \approx 1$), yellow color exhibits the spiral waves ($Z_L \approx 1$ and PS> 0) and gray color show the non-spiral waves ($Z_g < 0.75$, $Z_L \approx 1$ and PS$= 0$). Panel (a) shows that Z_g and the

wave pattern depend on the coupling strength, the network is globally synchronized for $0.01 < g_{syn} < 0.08$ nS. However, as g_{syn} increases the neurons globally desynchronize exhibiting non-spiral wave patterns and for further values spiral waves start to emerge. For $g_{syn} \geq 0.122$ nS the network presents bursting activity (CV > 0.5) and on the range $0.122 \leq g_{syn} \leq 0.126$ nS bursting synchronization is observed. Most of the non-spiral regions are immersed in the bursting region ($0.122 < g_{syn} < 0.21$ nS). Panel (b) displays the amount of the phase singularities (PS) as a function of the coupling strength. Multiple spirals appear depending on g_{syn}, and there is an increase of PS for values close to the spike-to-burst transition coupling strength $g_{syn} = 0.122$ nS.

Figure 30 – Panel (a) displays the mean global Kuramoto order parameter (Z_g) and (b) shows the coefficient of variation (CV) as a function of g_{syn} for $R = 75$ μm. The colors represent the wave pattern that emerges for that value of g_{syn} synchronization waves (red line), desynchronization (blue line), non-spiral waves (gray) and spiral waves (yellow). Simulation time = 37 minutes 26 seconds, cores = 10.

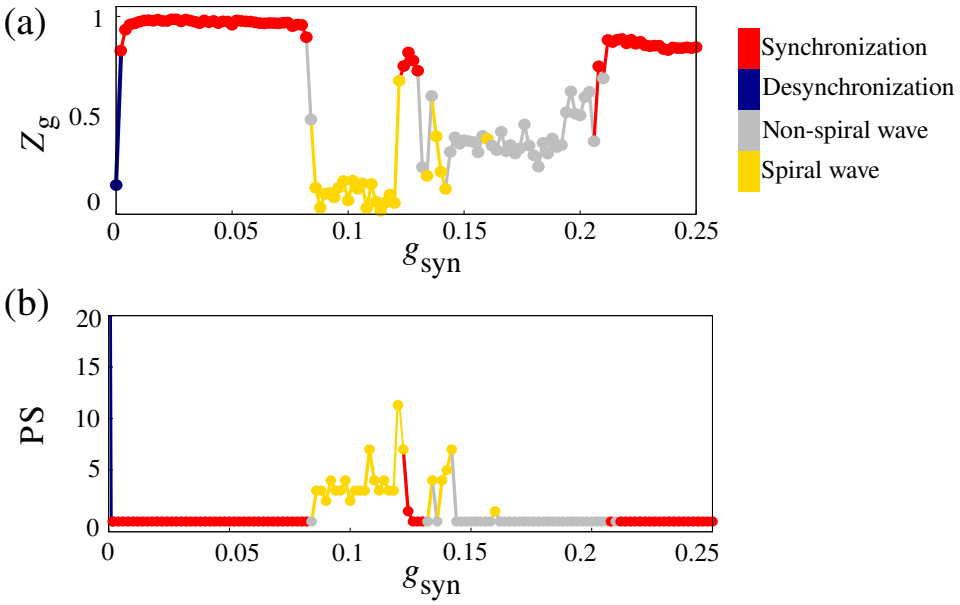

Source: the author.

Now, we explore the different wave patterns that are produced by combinations of (R, g_{syn}). Figure 31 displays the $R \times g_{syn}$ parameter space where the z-axis displays the global order parameter Z_g and the color scale represents the pattern observed in the network. For low values of R, the network displays desynchronization (no wave is observed), and a little increase in the radius of connection produces a yellow region where spiral waves are observable. There is a vast region of synchronization (red region) for a great amount of (R, g_{syn}) combinations. In the transition from spiral to synchronized wave, the network displays different wave patterns which we denominate as non-spiral waves. Most of the non-spiral waves are observed at $60 < R < 80$ μm and $0.18 < g_{syn} < 0.25$ nS, in this range, the network displays bursting CV> 0.5. The appearance of a burst spiral is intrinsically related to long-range connections (R ≥ 60 μm) and intense coupling strength ($g_{syn} \geq 0.12$ nS).

Figure 31 – Connection radius R and coupling strength g_{syn} parameter space where the z-axis depicts the global Kuramoto order parameter and the color scale represents the wave pattern desynchronization (blue color), synchronization wave (red color), spiral wave (yellow color) and non-spiral wave (gray color). Simulation run on Oscillations Control Group's server, simulation time = 52 hours 17 minutes, cores = 16.

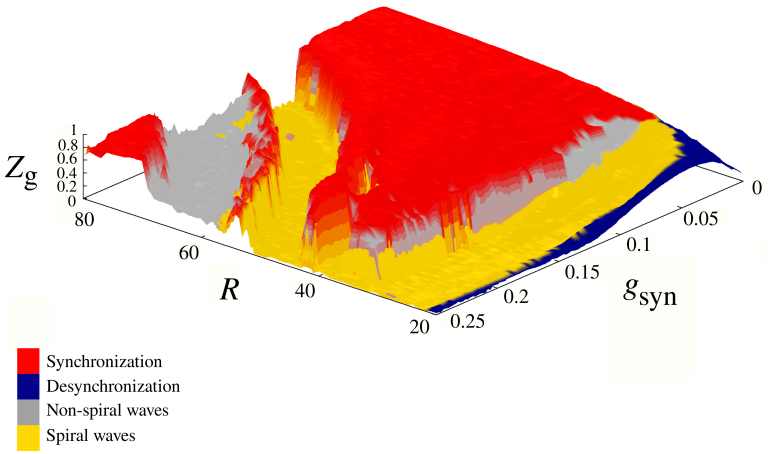

Source: the author.

4.3 INITIAL CONDITION AND BISTABILITY

Whether a chimera-like state appears spontaneously or not in the network depends on the initial condition considered (12, 90). In the previous sections, we consider fixed initial conditions for all our simulations therefore we avoid such dependence. In this section, we investigate the robustness of the wave patterns when considering different initial conditions. Now, the initial conditions $V_i(0)$ and $w_i(0)$ are randomly chosen at each simulation from the ranges $V_i(0) \in [-70, -45]$ mV and $w_i(0) \in [0, 70]$ pA, the values are determined by a random uniform generator. Firstly, we study the initial conditions' influence over the network for different coupling strength g_{syn}. In the last part of this section, we show the bistability regimes that appear in the network for specific g_{syn} ranges.

To investigate the initial condition impact in the network we consider ten independent simulations and calculate the arithmetic mean of the global order parameter Z_g, CV and PS. Figure 32 displays the mean values of Z_g (a), CV (b) and PS (c) as a function of g_{syn} with their respective error bars. The green dashed line separates the spike (CV<0.5) and burst (CV≥ 0.5) region, to determine the position of the transition spike-to-burst, we analyze the coefficient of variation CV, we consider $R = 75$ μm. The shape of Z_g in panel (a) is quite different from Figure 30 (a), mostly in the regions where the error bar is large. This occurs because Figure 30 (a) is considered one set of initial conditions. The synchronization pattern is shown to be robust to different initial conditions, and the error bar in this wave pattern does not vary much from the mean. The same cannot be stated for non-spiral waves, in this pattern, the global

synchronization strongly depends on the initial conditions. In the bursting region ($g_{syn} > 0.122$ nS), the non-spiral waves present great variation depending on the initial condition, and for some values of g_{syn} the pattern observed could be the synchronization instead of the non-spiral wave. The spike or burst firing pattern does not vary significantly for different sets of initial conditions, there is a greater variation in the spike-to-burst transition for $g_{syn} = 0.122$ nS. The mean amount of PS is displayed in panel (c). For the synchronization pattern $0.054 \leq g_{syn} \leq 0.086$ nS the number of PS measured does not vary for different initial conditions. The mean PS in the spiral waves region (yellow color) in the simulations is 1, however, this value greatly varies around the mean, for $g_{syn} = 0.118$ nS the amount of PS does not alter much. There is a great dispersion of the amount of PS during the non-spiral waves in the burst region. For $0.126 \leq g_{syn} \leq 0.150$ nS, the measurements of PS greatly vary around the mean, and there are simulations in which no burst spiral waves are observed although depending on the initial conditions, multiple burst spiral waves emerge in the network. The measurement of PS presents a small dispersion around the mean for $g_{syn} > 0.15$ nS. Panels (a) and (c) show that Z_g and PS, respectively, possess a great dispersion around their respective mean after the spike-to-burst transition. Most of the high dispersion points are concentrated for g_{syn} values near the burst synchronization (red line in the burst region).

Figure 32 – Mean value of Z_g (a), CV (b) and PS (c) of ten simulations with random initial conditions generated by a random uniform generator, the dispersion around the mean is represented by the error bars. We consider $R = 75$ μm. Simulation run on the Oscillations Control Group server, simulation time = 168 minutes 10 seconds, cores = 10.

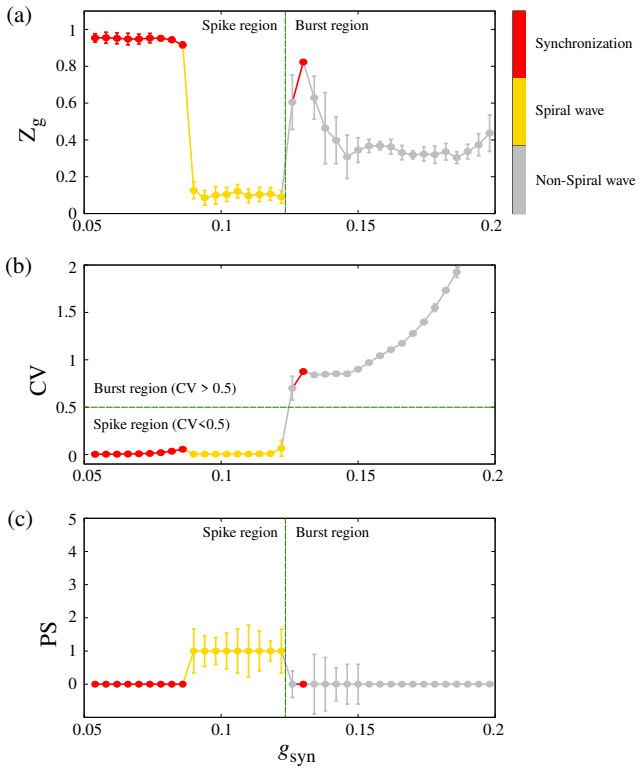

Source: the author.

Figure 33 displays the mean global Kuramoto order parameter Z_g (a) and the amount of PS in (b). The red dotted line displays the case in which the g_{syn} starts at 0.06 nS and its values increase. Meanwhile, the blue dotted line starts at $g_{syn} = 0.1$ nS and the coupling strength decreases. This type of plot is denominated as a hysteresis diagram (12, 16). In panels (a) and (b) a bistable regime is observable, in which two possible states are possible to be achieved depending on the first initial condition considered. Panel (a) shows that for a range of g_{syn} the network can be synchronized ($Z_g \approx 1$) or desynchronized ($Z_g \approx 0$). Parting from a synchronized initial condition, the synchronization is maintained for more values of g_{syn}, differently from the situation in which the initial conditions are asynchronous. Panel (b) displays that different wave patterns can be reached, spiral wave or synchronous wave, depending on the first set of initial conditions.

Figure 33 – Hysteresis diagram of (a) Z_g and (b) PS. Increasing values of g_{syn} are displayed in a red dotted line and the decreasing values of g_{syn} are depicted in a blue dotted line

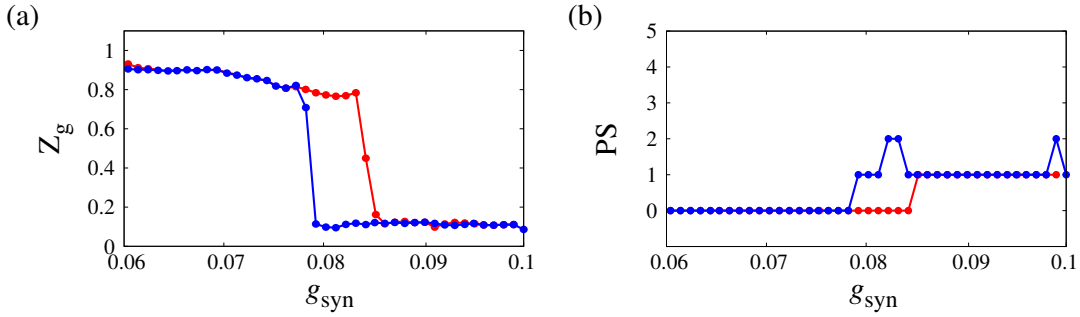

Source: the author.

5 CONCLUSIONS

In this dissertation, the excessive synchronization and the emergence of traveling chimera waves in a CA1 hippocampal excitatory layer were studied by the variation of the network parameters the radius of connection and the coupling strength. The individual dynamics of each neuron of our network were described by the adaptive exponential integrate-and-fire model (AEIF), which combines the biophysical accuracy of the mechanisms underlying the electrical activity of neurons and the simplicity of computational implementation in complex networks. The neurons were spatially distributed as one layer of excitatory neurons in the hippocampus CA1 region, we consider a 1000×1000 μm layer. Each neuron connects with a neighbor with a certain coupling strength if its distance is within a given radius of connection. By considering different values of the radius of connection and coupling strength, different firing patterns can emerge in the network, for instance, excessive synchronization and spiral waves. Since excessive synchronization is related to multiple brain disorders, understanding how the network parameters influence synchronization is essential to developing new approaches for such diseases. The spiral waves that appear in the brain are not yet fully understood, however, studies show the properties of such patterns are related to specific cognitive tasks. Therefore, comprehending this wave pattern dependence of the network and being able to detect such a pattern is crucial for further studies and insights into the roles of spiral waves in the brain. Additionally, we introduce a novel method capable of identifying chimera spiral waves.

We have shown that our network displays distinct firing patterns for different coupling strengths and radius of connection. We have shown that the synchronization of the spike firing pattern is easily achieved within our network. However, for some values of the radius of connection, a transition of spike-to-burst is observed when the coupling strength passes a specific value. Despite spike synchronization being easily achieved, the neurons globally desynchronize for values of coupling strength close to the transition spike-to-burst. We have associated the synchronization-to-desynchronization transition for some values of coupling strength with the high amount of synapses and the increased coupling strength between each neuron. For higher values of coupling strength, the network starts displaying a burst firing pattern with a higher frequency rate than the spike case. For specific values of coupling strength, the network burst synchronizes, state-related with epileptic seizures. For the radius of connection lower than 50 μm, the network does not exhibit bursting activity. The network presents local synchronization for most of the combination of the network parameters.

The synchronization tools, global and local Kuramoto order parameters, have shown to be great tools for wave detection. The shape, speed and other properties of each traveling wave vary, however, all of them leave a specific trace in the local order parameter. For all cases in which a traveling wave propagates in the network the mean local synchronization is almost 1 due to the fact that traveling waves appear when close neurons fire together, indicating that traveling waves facilitate the local dynamics. The mean global order parameter does not yield

much information regarding the presence of a traveling wave in the network, since there are global synchronous waves and globally asynchronous waves (for instance multi-rings and spiral waves). In the whole network, the passage of a wave facilitates local neurons to produce an action potential while neurons that are not in the wave trajectory do not receive firing support. These local characteristics of the waves can be used for detecting the presence of a wave in the network. Therefore, we proposed a diagnostic method for detecting traveling waves in the network. The waves (except synchronous rings) produce a low mean global order parameter and a high mean local order parameter. Applying these criteria, it is possible to detect the presence of a wave, however, this diagnostic does not provide information regarding the type of wave, except for the synchronous ring that is characterized by high mean global and local order parameters (close to 1).

In this work, we have focused our attention on the detection of spiral waves. We have proposed a novel methodology for the detection of spiral waves in the network. The spiral waves produce a specific phase abnormality in the core of the spiral, denominated as phase singularity (PS). The PS are composed of desynchronized neurons and they are the core of the spiral. The core of the spiral produces a local order parameter inferior to 0.7 where it is located. By plotting the local order parameter of each neuron the core is easily observed as an asynchronous spot amidst a local synchronized region. Thus, we have proposed that PS are characterized by a low local order parameter, inferior to 0.7, we theorize that for the generation of a spiral wave, its core must reach a "level of desynchronization". Multiple PS can coexist at the same time in the network, and the spirals can interact with each other, however, a great number of PSs promote global and local desynchronized activity. Therefore, we have defined a maximum number of PSs in the network equal to 20. We have proposed three conditions that must be met to observe spiral waves in the network, these conditions regard the range of both local and global order parameters and the amount of PSs. The mean global order parameter must point to desynchronized activity, the local order parameter must have at least one region inferior to 0.7 that is not in the border and the amount of PS cannot be superior to a certain maximum value. The spiral waves can appear as spike or burst firing patterns, spike spiral waves were obtained for a diverse range of radius of connection and coupling strength, although, burst spiral waves are restricted for very specific values of the network parameters.

We have also investigated how the wave patterns behave when considering different initial conditions since chimera states are intrinsically dependent on how the systems begin. We have observed that the firing pattern of the network is very robust for different initial conditions, and the coefficient of variation does not vary independently of the wave pattern. However, the mean global order parameter and the amount of PS have some dependences on the initial conditions. The network can present synchronized or asynchronous activity depending on the initial condition when the neurons present bursting activity. The amount of PS varies in the spiral wave pattern and also in the non-spiral wave pattern depending on the initial conditions considered. However, such variation in the amount of PS in the non-spiral wave only occurs for

values of coupling strength close to the burst synchronization point. By analysing the hysteresis diagram, we have observed that depending on the first set of initial conditions there are bistable regions for the global synchronization and the amount of PSs.

6 FUTURE WORKS

In future works, we intend to explore the effects of inhibitory neurons over the generation of traveling waves and the impact of inhibition on the emergence of spiral waves in the complete network of the CA1 hippocampus column (39). We also intend to investigate the influence of ionic channels on the emergence of traveling waves when considering a conductance-based model of Hodgkin-Huxley (16). Another future work is to understand the mechanisms underlying the generation of spiral waves in a biophysical reconstruction of a hemisphere of the hippocampus.

A possible future work is to investigate the response of the traveling waves to lesions and deformities in the network for instance a mechanical lesion or Alzheimer's.

REFERENCES

1 KANDEL, E. R.; SCHWARTZ, J. H.; JESSELL, T. M. **Principles of Neural Science**. 5th. ed. New York: Elsevier, 2013.

2 CARLOS, J. A. D.; BORRELL, J. A historical ref ection of the contributions of cajal and golgi to the foundations of neuroscience. **Brain Research Reviews**, v. 55, p. 8–16, 2007.

3 CAJAL, S. R. Estructura de los centros nerviosos de las aves. **Revista Trimestral de Histología Normal y Patológica**, v. 1, p. 1–10, 1888.

4 CAJAL, S. R. Leyes de la morfología y dinamismo de las células nerviosas. **Imprenta y Librería de Nicolás Moya**, 1897.

5 BARBERIS, S. D. Cajal's law of dynamic polarization: Mechanism and design. **Philosophies**, v. 3, p. 11, 2018.

6 LENT, R. **Cem bilhões de neurônios?: conceitos fundamentais da neurociência**. 2nd. ed. São Paulo: Atheneu, 2003.

7 NOBACK, C. R.; STROMINGER, N. L.; DEMARES R. J. ABD RUGGIERO, D. A. **The Human Nervous System: Structure and Function**. 6th. ed. [S.l.]: Humana Press, 2005.

8 MULLER, L.; CHAVANE, F.; REYNOLDS, J.; SEJNOWSKI, T. J. Cortical travelling waves: mechanisms and computational principles. **Nature Reviews Neuroscience**, v. 19, n. 5, p. 255–268, 2018.

9 ZHANG, H.; JACOBS, J. Traveling theta waves in the human hippocampus. **Journal of Neuroscience**, v. 35, n. 36, p. 12477–12487, 2015.

10 LUBENOV, E. V.; SIAPAS, A. G. Hippocampal theta oscillations are travelling waves. **Nature**, v. 459, n. 7246, p. 534–539, 2009.

11 BUZSÁKI, G. **Rhythms of the Brain**. Oxford: Oxford university press, 2006.

12 SOUZA, D. L. M.; BORGES, F. S.; GABRICK, E. C.; BENTIVOGLIO, L. E.; PROTACHEVICZ, P. R.; SANTOS, V.; VIANA, R. L.; CALDAS, I. L.; IAROSZ, K. C.; BATISTA, A. M.; KURTHS, J. Spiral wave dynamics in a neuronal network model. **Journal of Physics: Complexity**, v. 5, n. 2, p. 025010, 2024.

13 PROTACHEVICZ, P. R.; BORGES, F. S.; LAMEU, E. L.; JI, P.; IAROSZ, K. C.; KIHARA, A. H.; CALDAS, I. L.; SZEZECH, J. D.; BAPTISTA, M. S.; MACAU, E. E. N.; ANTONOPOULOS, C. G.; BATISTA, A. M.; KURTHS, J. Bistable f ring pattern in a neural network model. **Frontiers in Computational Neuroscience**, v. 13, 2019.

14 BORGES, F. S.; GABRICK, E. C.; PROTACHEVICZ, P. R.; HIGA, G. S. V.; LAMEU, E. L.; RODRIGUEZ, P. X. R.; FERRAZ, M. S. A.; JR, J. D. S.; BATISTA, A. M.; KIHARA, A. H. Intermittency properties in a temporal lobe epilepsy model. **Epilepsy & Behavior**, v. 139, p. 109072, 2023.

15 ARENAS, A.; DÍAZ-GUILERA, A.; KURTHS, J.; MORENO, Y.; ZHOU, C. Synchronization in complex networks. **Physics reports**, v. 469, n. 3, p. 93–153, 2008.

16 BORGES, F. S.; PROTACHEVICZ, P. R.; SOUZA, D. L. M.; BITTENCOURT, C. F.; GABRICK, E. C.; BENTIVOGLIO, L. E.; SZEZECH, J. D. J.; BATISTA, A.; CALDAS, I. L.; DURA-BERNAL, S.; PENA, R. The roles of potassium and calcium currents in the bistable firing transition. **Brain Science**, v. 13, p. 1347, 2023.

17 JIRUSKA, P.; CURTIS, M. D.; JEFFERYS, J. G. R.; SCHEVON, C. A.; SCHIFF, S. J.; SCHINDLER, K. Synchronization and desynchronization in epilepsy: controversies and hypotheses. **The Journal of physiology**, Wiley Online Library, v. 591, n. 4, p. 787–797, 2013.

18 LI, X.; CUI, D.; JIRUSKA, P.; FOX, J. E.; YAO, X.; JEFFERYS, J. G. R. Synchronization measurement of multiple neuronal populations. **Journal of neurophysiology**, American Physiological Society, v. 98, n. 6, p. 3341–3348, 2007.

19 WU, Y.; LIU, D.; SONG, Z. Neuronal networks and energy bursts in epilepsy. **Neuroscience**, v. 287, p. 175–186, 2015.

20 MCCANDLESS, D. W. **Epilepsy: animal and human correlations**. [S.l.]: Springer Science & Business Media, 2011.

21 TRAUB, R. D.; JEFFERYS, J. G. R.; WHITTINGTON, M. A. Enhanced nmda conductance can account for epileptiform activity induced by low mg2+ in the rat hippocampal slice. **Journal of Physiology**, v. 478, p. 379–393, 1994.

22 WHITE, H. S. Animal models of epileptogenesis. **Neurology**, v. 59, n. 9, p. 7–14, 2002.

23 PATTEN, T. M.; RENNIE, C. J.; ROBINSON, P. A.; GONG, P. Human cortical traveling waves: Dynamical properties and correlations with responses. **PLoS ONE**, v. 7, n. 6, p. e38392, 2012.

24 XU, Y.; LONG, Y.; FENG, J.; GONG, P. Interacting spiral wave patterns underlie complex brain dynamics and are related to cognitive processing. **Nature Human Behaviour.**, v. 7, p. 1196–1215, 2023.

25 IZHIKEVICH, E. M. **Dynamical Systems in Neuroscience: The Geometry of Excitability and Bursting**. 1st. ed. Cambridge: The MIT Press, 2006.

26 IZHIKEVICH, E. M. Simple model of spiking neurons. **IEEE Transactions on Neural Network**, v. 14, n. 6, p. 1596–1572, 2003.

27 RULKOV, N. F. Modeling of spiking-bursting neural behavior using two-dimensional map. **Physical Review E**, v. 65, n. 4, p. 041922, 2002.

28 HODGKIN, A. L.; HUXLEY, A. F. A quantitative description of membrane current and its application to conduction and excitation in nerve. **Journal of Physiology**, v. 117, p. 500–544, 1952.

29 HINDMARSH, J. L.; ROSE, R. M. A model of neuronal bursting using three coupled first order differential equations. **Proceedings of the Royal society of London. Series B. Biological sciences**, v. 221, n. 1222, p. 87–102, 1984.

30 LV, G.; ZHANG, N.; MA, K.; WENG, J.; ZHU, P.; CHEN, F.; HE, G. Functional brain network dynamics based on the hindmarsh–rose model. **Nonlinear Dynamics**, v. 104, p. 1475–1489, 2021.

31 ABBOTT, L. F. Lapicque's introduction of the integrate-and-fire model neuron (1907). **Brain Research Bulletin**, v. 50, n. 5-6, p. 303–304, 1999.

32 OSTOJIC, S.; BRUNEL, N. From spiking neuron models to linear-nonlinear models. **PLoS computational biology**, v. 7, n. 1, p. e1001056, 2011.

33 BRETTE, R.; GERSTNER, W. Adaptive exponential integrate-and-fire model as an effective description of neuronal activity. **Journal of neurophysiology**, v. 94, n. 5, p. 3637–3642, 2005.

34 NAUD, R.; MARCILLE, N.; CLOPATH, C.; GERSTNER, W. Firing patterns in the adaptive exponential integrate-and-fire model. **Biological cybernetics**, v. 99, p. 335–347, 2008.

35 SOUZA, D. L. M.; GABRICK, E. C.; PROTACHEVICZ, P. R.; BORGES, F. S.; TROBIA, J.; IAROSZ, K. C.; BATISTA, A. M.; CALDAS, I. L.; LENZI, E. K. Adaptive exponential integrate-and-fire model with fractal extension. **Chaos: An Interdisciplinary Journal of Nonlinear Science**, v. 34, n. 2, p. 023107, 2024.

36 HODGKIN, A. L.; HUXLEY, A. F.; KATZ, B. Measurement of current-voltage relations in the membrane of the giant axon of loligo. **The Journal of Physiology**, v. 116, p. 424–448, 1952.

37 GERSTNER, W.; AL. et. **Neuronal Dynamics: From Single Neurons to Networks and models of Cognition**. 1st. ed. Cambridge: Cambridge University Press, 2014.

38 BEZAIRE, M. J.; SOLTESZ, I. Quantitative assessment of ca1 local circuits: knowledge base for interneuron-pyramidal cell connectivity. **Hippocampus**, v. 23, n. 9, p. 751–785, 2013.

39 BEZAIRE, M. J.; RAIKOV, I.; BURK, K.; VYAS, D.; SOLTESZ, I. Interneuronal mechanisms of hippocampal theta oscillations in a full-scale model of the rodent ca1 circuit. **Elife**, v. 5, p. e18566, 2016.

40 SANTOS, M. S.; PROTACHEVICZ, P. R.; CALDAS, I. L.; IAROSZ, K. C.; VIANA, R. L.; SZEZECH, J. D.; SOUZA, S. L. T. de; BATISTA, A. M. Spiral wave chimera states in regular and fractal neuronal networks. **Journal of Physics: Complexity**, v. 2, n. 1, p. 015006, 2020.

41 KURAMOTO, Y. **Chemical oscillations, waves, and turbulence**. Berlin: Springer-Verlag, 1984.

42 STROGATZ, S. H. **Nonlinear dynamics and chaos: with applications to physics, biology, chemistry, and engineering**. [S.l.]: CRC press, 2018.

43 TROBIA, J.; TIAN, K.; BATISTA, A. M.; GREBOGI, C.; REN, H.-P.; SANTOS, M. S.; PROTACHEVICZ, P. R.; BORGES, F. S.; JR, J. D. S.; VIANA, R. L. et al. Mathematical model of brain tumour growth with drug resistance. **Communications in Nonlinear Science and Numerical Simulation**, v. 103, p. 106013, 2021.

44 GABRICK, E. C.; PROTACHEVICZ, P. R.; BATISTA, A. M.; IAROSZ, K. C.; SOUZA, S. L. de; ALMEIDA, A. C.; JR, J. D. S.; MUGNAINE, M.; CALDAS, I. L. Effect of two vaccine doses in the seir epidemic model using a stochastic cellular automaton. **Physica A: Statistical Mechanics and its Applications**, v. 597, p. 127258, 2022.

45 EVARISTO, R. M.; BATISTA, A. M.; VIANA, R. L.; IAROSZ, K. C.; JR, J. D. S.; GODOY, M. F. de. Mathematical model with autoregressive process for electrocardiogram signals. **Communications in Nonlinear Science and Numerical Simulation**, v. 57, p. 415–421, 2018.

46 ALLIGOOD, K. T.; SAUER, T. D.; YORKE, J. A.; CHILLINGWORTH, D. **Chaos: an introduction to dynamical systems**. New York: Springer, 1996.

47 ERDOS, P. On the evolution of random graphs. **Bulletin of the Institute of International Statistics**, v. 38, p. 343–347, 1961.

48 WATTS, D. J.; STROGATZ, S. H. Collective dynamics of 'small-world'networks. **Nature**, v. 393, n. 6684, p. 440–442, 1998.

49 BARABÁSI, A.; ALBERT, R. Emergence of scaling in random networks. **Science**, v. 286, n. 5439, p. 509–512, 1999.

50 MILGRAM, S. The small world problem. **Psychology today**, v. 2, n. 1, p. 60–67, 1967.

51 NEWMAN, M. E. J.; WATTS, D. J. Scaling and percolation in the small-world network model. **Physical review E**, v. 60, n. 6, p. 7332, 1999.

52 LLINáS, R. R. The contribution of santiago ramón y cajal to functional neuroscience. **Brain Research Reviews**, v. 4, p. 77–80, 2003.

53 SHIMOURA, R. O.; PENA, R. F. O.; KAMIJI, N. L.; LIMA, V.; ROQUE, A. C. Modelos de redes de neurônios para o neocórtex e fenômenos emergentes observados. **Revista Brasileira de Ensino de Física**, v. 43, p. e20200452, 2021.

54 SIEGEL, A.; SAPRU, H. N. **Essential Neuroscience**. 3rd. ed. Philadelphia: Lippicott Williams & Wilkins, 2015.

55 ARBIB, M. A. **The Handbook of Brain Theory and Neural Networks**. 2nd. ed. Cambridge: The MIT Press, 2002.

56 DUBOIS, J.; OUANOUNOU, G.; ROUZAIRE-DUBOIS, B. The boltzmann equation in molecular biology. **Progress in Biophysics and Molecular Biology**, v. 99, p. 87–93, 2009.

57 ATKINS, P.; PAULA, J. de. **Physical Chemistry**. 8th. ed. Oxford: W. H. Freeman and Company, 2006.

58 SEIFTER, J.; SLOANE D.AND RATNER, A. **Concepts in medical physiology**. Philadelphia: Lippincott Williams & Wilkins, 2005.

59 BRODAL, P. **The central nervous system**. 4th. ed. Oxford: Institute of Basic Medical Sciences, 2010.

60 DALE, H. H. Pharmacology and nerve endings. **Proceedings of the Royal Society of Medicine**, v. 28, p. 303–323, 1935.

61 HERTäG, L.; HASS, J.; GOLOVKO, T.; DURSTEWITZ, D. An approximation to the adaptive exponential integrate-and-fire neuron model allows fast and predictive fitting to physiological data. **Frontiers in Computational Neuroscience**, v. 6, 2012.

62 TEETER, C.; IYER, R.; MENON, V.; GOUWENS, N.; FENG, D.; BERG, J.; SZAFER, A.; CAIN, N.; ZENG, H.; HAWRYLYCZ, M. et al. Generalized leaky integrate-and-fire models classify multiple neuron types. **Nature communications**, v. 9, n. 1, p. 709, 2018.

63 HODGKIN, A. L.; HUXLEY, A. F. Action potentials recorded from inside a nerve fibre. **Nature**, v. 144, p. 710–711, 1939.

64 SCHWIENING, C. J. A brief historical perspective: Hodgkin and huxley. **Journal of Physiology**, v. 590, p. 2571–2575, 2012.

65 HODGKIN, A. L.; HUXLEY, A. F. Resting and action potentials in single nerve fibres. **Journal of Physiology**, v. 104, p. 176–195, 1945.

66 HODGKIN, A. L.; HUXLEY, A. F. Propagation of electrical signals along giant nerve fibres. **Proc. R. Soc. Lond. B. Biol. Sci.**, v. 140, p. 177–183, 1952.

67 HODGKIN, A. L.; HUXLEY, A. F. Currents carried by sodium and potassium ions through the membrane of the giant axon of loligo. **Journal of Physiology**, v. 116, p. 449–472, 1952.

68 HODGKIN, A. L.; HUXLEY, A. F. The components of membrane conductance in the giant axon of loligo. **Journal of Physiology**, v. 116, p. 473–496, 1952.

69 HODGKIN, A. L.; HUXLEY, A. F. The dual effect of membrane potential on sodium conductance in the giant axon of loligo. **Journal of Physiology**, v. 116, p. 497–506, 1952.

70 TOUBOUL, J.; BRETTE, R. Dynamics and bifurcations of the adaptive exponential integrate-and-fire model. **Biological cybernetics**, v. 99, n. 4, p. 319–334, 2008.

71 CLOPATH, C.; JOLIVET, R.; RAUCH, A.; LÜSCHER, H.-R.; GERSTNER, W. Predicting neuronal activity with simple models of the threshold type: Adaptive exponential integrate-and-fire model with two compartments. **Neurocomputing**, v. 70, n. 10-12, p. 1668–1673, 2007.

72 SHIAU, L.; BUHRY, L. Interneuronal gamma oscillations in hippocampus via adaptive exponential integrate-and-fire neurons. **Neurocomputing**, v. 331, p. 220–234, 2019.

73 NGHIEM, T.-A. E.; TORT-COLET, N.; GÓRSKI, T.; FERRARI, U.; MOGHIMY-FIROOZABAD, S.; GOLDMAN, J. S.; TELEŃCZUK, B.; CAPONE, C.; BAL, T.; VOLO, M. D. et al. Cholinergic switch between two types of slow waves in cerebral cortex. **Cerebral Cortex**, v. 30, n. 6, p. 3451–3466, 2020.

74 SHRIKI, O.; HANSEL, D.; SOMPOLINSKY, H. Rate models for conductance-based cortical neuronal networks. **Neural computation**, v. 15, n. 8, p. 1809–1841, 2003.

75 LISMAN, J. E.; JENSEN, O. The theta-gamma neural code. **Neuron**, v. 77, n. 6, p. 1002–1016, 2013.

76 TRAUB, R. D.; MILES, R. *Neuronal networks of the hippocampus*. [S.l.]: Cambridge University Press, 1991. v. 777.

77 GRAVES, A. R.; MOORE, S. J.; BLOSS, E. B.; MENSH, B. D.; KATH, W. L.; SPRUSTON, N. Hippocampal pyramidal neurons comprise two distinct cell types that are countermodulated by metabotropic receptors. **Neuron**, v. 76, n. 4, p. 776–789, 2012.

78 WOODSON, W.; NITECKA, L.; BEN-ARI, Y. Organization of the gabaergic system in the rat hippocampal formation: a quantitative immunocytochemical study. **Journal of Comparative Neurology**, v. 280, n. 2, p. 254–271, 1989.

79 AIKA, Y.; REN, J. Q.; KOSAKA, K.; KOSAKA, T. Quantitative analysis of gaba-like-immunoreactive and parvalbumin-containing neurons in the ca1 region of the rat hippocampus using a stereological method, the disector. **Experimental brain research**, v. 99, p. 267–276, 1994.

80 PIKOVSKY, A.; ROSENBLUM, M.; KURTHS, J. **Synchronization: A universal concept in nonlinear sciences**. [S.l.]: Cambridge University Press, 2001.

81 SOUZA, D. L. M. *Dissertation repositorie*. 2024. Accessed on May 27th, 2024. Disponível em: <https://github.com/DiogoLeonai/Dissertation>.

82 OMELCHENKO, I.; OMEL'CHENKO, E.; HÖVEL, P.; SCHÖLL, E. When nonlocal coupling between oscillators becomes stronger: patched synchrony or multichimera states. **Physical review letters**, v. 110, n. 22, p. 224101, 2013.

83 ABRAMS, D. M.; STROGATZ, S. H. Chimera states for coupled oscillators. **Physical review letters**, APS, v. 93, n. 17, p. 174102, 2004.

84 SETHIA, G. C.; SEN, A.; JOHNSTON, G. L. Amplitude-mediated chimera states. **Physical Review E—Statistical, Nonlinear, and Soft Matter Physics**, APS, v. 88, n. 4, p. 042917, 2013.

85 STROGATZ, S. *Sync: The emerging science of spontaneous order*. [S.l.]: Penguin UK, 2004.

86 GLAZE, T. A.; LEWIS, S.; BAHAR, S. Chimera states in a hodgkin-huxley model of thermally sensitive neurons. **Chaos: An Interdisciplinary Journal of Nonlinear Science**, AIP Publishing, v. 26, n. 8, 2016.

87 HAUGLAND, S. W. The changing notion of chimera states, a critical review. **Journal of Physics: Complexity**, IOP Publishing, v. 2, n. 3, p. 032001, 2021.

88 LI, T.; PAN, D.; ZHOU, K.; JIANG, R.; JIANG, C.; ZHENG, B.; ZHANG, H. Jacobian-determinant method of identifying phase singularity during reentry. **Physical Review E**, v. 98, n. 6, p. 062405, 2018.

89 DING, Q.; WU, Y.; HU, Y.; LIU, C.; HU, X.; JIA, Y. Tracing the elimination of reentry spiral waves in defibrillation: Temperature effects. **Chaos, Solitons & Fractals**, v. 174, p. 113760, 2023.

90 FAGHANI, Z.; ARAB, Z.; PARASTESH, F.; JAFARI, S.; PERC, M.; SLAVINEC, M. Effects of different initial conditions on the emergence of chimera states. **Chaos, Solitons & Fractals**, v. 114, p. 306–311, 2018.